Determining the Criticality of Li-Excess for Disordered-Rocksalt Li-Ion Battery Cathodes

Jinhyuk Lee,* Chao Wang, Rahul Malik, Yanhao Dong, Yimeng Huang, Dong-Hwa Seo,* and Ju Li*

The development of Li-excess disordered-rocksalt (DRX) cathodes for Li-ion batteries and interpretation through the framework of percolation theory of Li diffusion have steered researchers to consider "Li-excess" ($x > 1.1$ in $Li_xTM_{2-x}O_2$; TM = transition metal) as being critical to achieving high performance. It is shown that this is not necessary for Mn-rich DRX-cathodes demonstrated by $Li_{1.05}Mn_{0.90}Nb_{0.05}O_2$ and $Li_{1.20}Mn_{0.60}Nb_{0.20}O_2$, which both deliver high capacity (>250 mAh g^{-1}) regardless of their Li-excess level. By contextualizing this finding within the broader space of DRX chemistries and confirming with first-principles calculations, it is revealed that the percolation effect is not crucial at the nanoparticle scale. Instead, Li-excess is necessary to lower the charging voltage (through the formation of condensed oxygen species upon oxygen oxidation) of certain DRX cathodes, which otherwise would experience difficulties in charging due to their very high TM-redox potential. The findings reveal the dual roles of Li-excess – modifying the cathode voltage in addition to promoting Li diffusion through percolation – that must be simultaneously considered to determine the criticality of Li-excess for high-capacity DRX cathodes.

Prof. J. Lee, Dr. C. Wang, Dr. Y. Dong, Prof. J. Li
Department of Nuclear Science and Engineering
Massachusetts Institute of Technology
Cambridge, MA 02139, USA
E-mail: liju@mit.edu

Prof. J. Lee
Department of Mining and Materials Engineering
McGill University
Montreal, QC H3A 0C5, Canada
E-mail: jinhyuk.lee@mcgill.ca

Dr. C. Wang
School of Materials Science and Engineering
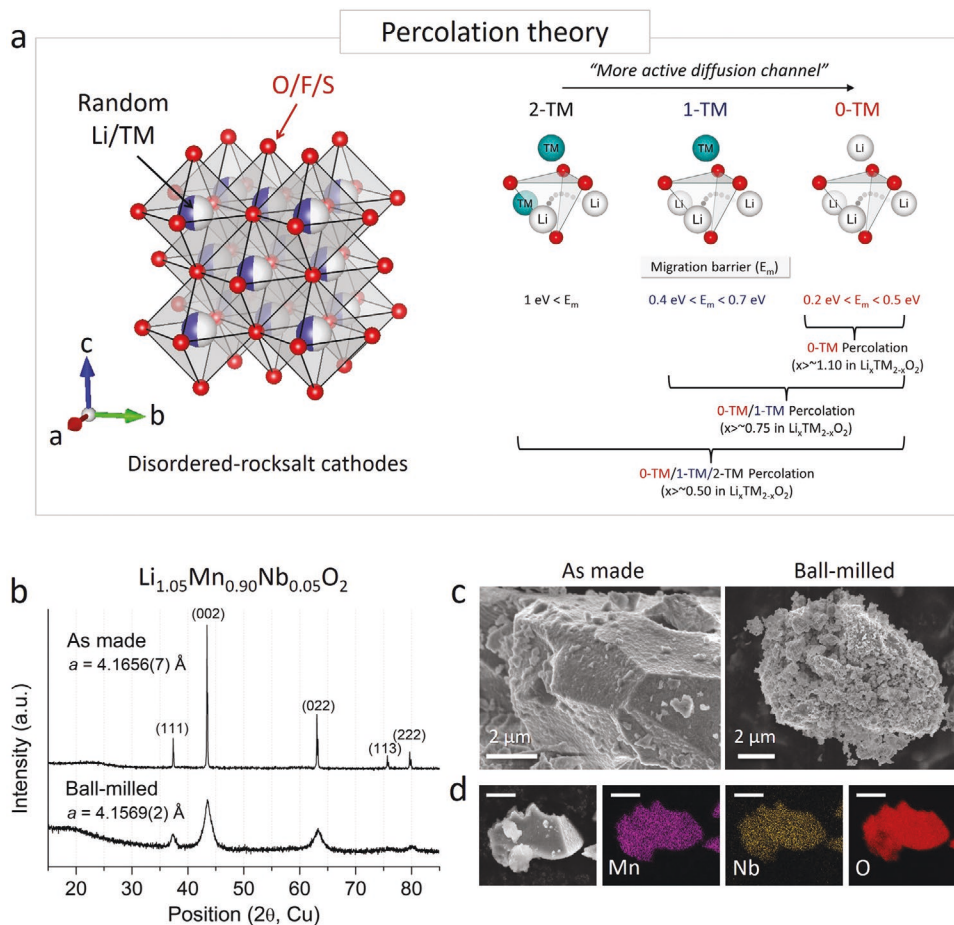Tongji University
Shanghai 201804, China

Dr. R. Malik
CAMX Power LLC
Lexington, MA 02421, USA

Y. Huang, Prof. J. Li
Department of Materials Science and Engineering
Massachusetts Institute of Technology
Cambridge, MA 02139, USA

Prof. D.-H. Seo
Department of Energy Engineering
School of Energy and Chemical Engineering
Ulsan National Institute of Science and Technology (UNIST)
Ulsan 44919, Republic of Korea
E-mail: dseo@unist.ac.kr

1. Introduction

While there remains an urgent need for low-cost and high-energy-density cathode materials for Li-ion batteries, the chemical and structural space to design from is increasingly restrictive.[1,2] The recent discovery and development of cathode materials with hybrid anionic and cationic redox (HACR) enabled through Li-excess composition revealed a new approach to achieve high capacity and energy density.[3–5] In particular, Mn-rich HACR cathodes are attractive due to the low cost and earth abundance of Mn compared to Ni or Co, which are the primary transition metals (TM) in conventional cathode materials (e.g., $LiCoO_2$).[2,6] The best known Mn-rich HACR cathodes have been the layered Li- and Mn-rich oxides (e.g., $Li_{1.2}Ni_{0.13}Mn_{0.54}Co_{0.13}O_2$).[7–9] Meanwhile, recent discoveries of high-capacity disordered-rocksalt (DRX)-type cathodes also raised substantial interest in developing the DRX-type Mn-rich HACR cathodes, such as $Li_2Mn_{2/3}Nb_{1/3}O_2F$, as well as compositions with other TMs (e.g., $Li_{1.2}Fe_{0.4}Ti_{0.4}O_2$).[10–30] These materials can be made with a wide variety of cations (e.g., Li, Na, Ti, V, Cr, Mn, Fe, Ni, Co, Nb, Zr, Mo, W, Ta) and anions (e.g., O, F, S), which considerably broadens the chemical space of possible high-energy cathodes.[10–30] Also, many DRX-cathodes do not experience the issue of low first-cycle coulombic efficiency,[10,12,21,22,28] which is a critical drawback of the layered Li- and Mn-rich cathodes.[8,9]

The recent interest in DRX-cathodes grew from observations that DRX Li-TM oxides with Li-excess compositions (e.g., $x = 1.2$ in $Li_xTM_{2-x}O_2$) could deliver superior capacities (>250 mAh g^{-1}), while those without Li-excess (e.g., $x = 1.0$ in $Li_xTM_{2-x}O_2$) typically showed limited performance (<100 mA g^{-1}).[10,15,16,31–33] Theoretical studies attribute the difference in performance to percolation of the so-called "0-TM channels" (0-TM percolation), which promotes Li diffusion in the DRX-cathodes, only possible if the degree of Li-excess exceeds a critical threshold (e.g., $x > 1.1$ in $Li_xTM_{2-x}O_2$; note that this percolation threshold can vary with the short-range ordering).[10,11,23] In the DRX structure, there are tetrahedral sites that share faces with zero TM (0-TM), one TM (1-TM), or two TM-cations (2-TM), which can connect two neighboring octahedral Li-sites (**Figure 1**a). Because TMs in the cathodes are in a high-valent state (e.g., $TM^{3+,4+}$), thus repulsive to Li$^+$-ions, the absence of a face-sharing TM-cation leads to a lower migration barrier for Li$^+$ when it

Figure 1. a) The schematic of the disordered-rocksalt cathode structure and explanation of the percolation theory, illustrating types of Li-diffusion channels (0-/1-/2-TM), migration barriers, and percolation thresholds under different assumptions.[10,11] b) X-ray diffraction patterns of $Li_{1.05}Mn_{0.90}Nb_{0.05}O_2$ (M90) before and after ball-milling. c) Scanning electron microscopy images of the as-made and ball-milled M90. d) The elemental mapping (Mn, Nb, and O) on an as-made M90-particle via energy-dispersive-X-ray spectroscopy. Scale bar: 2 µm

diffuses through the 0-TM tetrahedral site (0-TM channel), compared with 1-TM or 2-TM channels that are considered nearly inactive due to their high Li-migration barriers.[10,11] Thus, improved Li-transport kinetics due to percolation of the 0-TM channels enabled by Li-excess has been considered critical to achieving high capacity in DRX cathodes. Indeed, DRX Li-Ni-Ti-Mo-oxides and Li-Fe-Ti-oxides were designed on this basis and showed significant improvement in their reversible capacity as the Li-excess level was increased.[15,16] Moreover, besides oxides, various Li-excess DRX oxyfluorides and sulfides were developed (e.g., Li_3NbS_4, Li_2VO_2F), achieving ultrahigh capacity (≈300 mAh g^{-1}).[12,18,19,21,28] Based on these findings, the Li-excess strategy for 0-TM percolation has become a de facto design principle of the DRX cathodes.

While introducing Li-excess facilitates 0-TM percolation, it raises the initial average TM valence and thus may trade the theoretical TM cation-redox capacity for O anion-redox capacity, as demonstrated in many Li-rich cathodes shown to operate on oxygen redox as an additional electron reservoir.[13–17,21,22,34–37] O-redox provides an alternative source of reversible capacity. However, it comes with significant risk because the O-redox can reduce the oxygen-migration potential-energy barriers

(from 2.3–4.0 eV of O^{2-} to 0.9 eV of O^{1-} in the case of $Li_{2-x}MnO_3$ according to Lee and Persson).[38] Thus, both local oxygen mobility (LOM) and global oxygen mobility (GOM) are possible at room temperature in the cathode crystal, which can induce permanent structural damage (e.g., O loss from surface, pore creation).[5,8,9,20,36,37] Indeed, Li-excess DRX cathodes have shown poor capacity retention upon extended cycling.[13,14,16,21,22] Consequently, recent efforts reported in the DRX cathode literature have concentrated on minimizing the GOM-triggered structural damage that is coupled with improving the Li-transport through a high-level of Li-excess.[20,21,28,39] For instance, F-substitution for O could enhance the capacity retention of the Li-excess DRX oxides (e.g., $Li_{1.2}Mn_{0.6}Nb_{0.2}O_2 \rightarrow Li_{1.2}Mn_{0.7}Nb_{0.1}O_{1.8}F_{0.2}$) by increasing the TM-redox capacity at a given Li-excess level.[20,39] Also, Nb-doping and $LiNbO_3$-surface modification have been shown to enhance the performance of the DRX Li-excess Ni-Ti/Mo oxides.[40,41]

In this work, we demonstrate in a case study of $Li_{1.05}Mn_{0.90}Nb_{0.05}O_2$ (M90) and $Li_{1.2}Mn_{0.60}Nb_{0.20}O_2$ (M60) that once the particle size is sufficiently reduced, the Mn-rich DRX cathodes cycle well regardless of the Li-excess level, effectively removing the Li-excess "constraint" without sacrificing capacity

**ADVANCED
SCIENCE NEWS**

www.advancedsciencenews.com

**ADVANCED
ENERGY
MATERIALS**

www.advenergymat.de

and also mitigating the O-redox-triggered side reactions. Both M90 and M60 were first synthesized into DRX cathodes using a solid-state method and were then mechanically pulverized to have a small particle size below ≈150 nm. Although the low Li-excess level (5%) in M90 is well below the calculated 0-TM percolation threshold,[10,11] M90 can deliver similarly high capacity (≈250 mAh g^{-1}) and rate capability (≈185 mAh g^{-1} at 400 mA g^{-1}) as M60 with a Li-excess level (20%) above the percolation threshold. Furthermore, capacity-voltage retention is substantially better for M90 than M60.

Our finding that Li-excess is not critical for cycling Mn-rich DRX-cathodes with small particles motivates addressing why other DRX cathodes with different chemistries, such as Li-Ni-Ti-Mo oxides or Li-Fe-Ti oxides, do require a high level of Li-excess to achieve high capacity, even with nano-sized active particles. By contextualizing our results with other reports from the DRX literature and confirming with density functional theory (DFT) calculations, we elucidate that the 0-TM percolation is not critical at the nanoparticle scale. Instead, Li-excess is necessary to decrease the thermodynamic anion-redox voltages of certain DRX cathodes (Ni/Co/Fe-based DRX), which otherwise would face difficulties in charging due to their higher and more spread-out redox potentials (see Section 2.5). Overall, introducing Li-excess in DRX cathodes modifies the thermodynamic cathode voltage in addition to facilitating Li diffusion through 0-TM percolation, and both effects must be carefully considered together to design for high capacity.

2. Results and Discussion

2.1. Synthesis and Characterization of Mn-Rich DRX Compounds

$Li_{1.05}Mn_{0.90}Nb_{0.05}O_2$ (M90: 5%-Li-excess) and $Li_{1.20}Mn_{0.60}Nb_{0.20}O_2$ (M60: 20%-Li-excess) were selected as representative Mn-rich DRX compounds with insufficient (M90) and sufficient (M60) Li-excess for 0-TM percolation (percolation threshold ≈10% Li-excess).[10,11] These materials were made with a solid-state method (see the Method section) and can be considered as solid-solution compounds between $Li^+Mn^{3+}O^{2-}_2$ and $Li^+_3Nb^{5+}O^{2-}_4$ [$x = 5$ (M90) or 20 (M60) in $Li^+_{1+(x/100)}Mn^{3+}_{1-(x/50)}Nb^{5+}_{(x/100)}O^{2-}_2$] as discussed in earlier papers.[13,14] Nb^{5+} is already in its highest oxidation state in these compounds, thus cannot contribute to the charging capacity. As a result, Li-Mn-Nb-O cathodes are known to operate on Mn^{3+}/Mn^{4+} and O-redox.[13,14] In principle, pure cationic Mn^{3+}/Mn^{4+} redox would lead to a theoretical Mn-capacity of 258.33 mAh g^{-1} for M90 and 175.04 mAh g^{-1} for M60 to use before O-redox. We chose M90 to represent the Mn-rich compounds without the 0-TM percolation instead of the ones with even less Li-excess (i.e., $Li_{1.02}Mn_{0.96}Nb_{0.02}O_2$; 2%-Li-excess) because it was the least Li-excess Mn–Nb DRX oxide that we could synthesize successfully using the conventional solid-state synthesis method. The elemental analysis via inductively coupled plasma optical emission spectrometry (ICP-OES) shows that the actual Li: Mn: Nb atomic ratio is 1.071: 0.883: 0.046 for M90 and 1.233: 0.583: 0.184 for M60.

Figure 1b shows the X-ray diffraction (XRD) patterns of the as-made and ball-milled M90 samples. We observe well-defined peaks of a disordered-rocksalt phase from the XRD pattern of the as-made M90 powder. $LiMnO_2$ is known to form into either an orthorhombic (space group: *Pmnm*) or monoclinic (*C*2/*m*) phase,[29,42] and its DRX-polymorph (*Fm-3m*) could be made only through the mechanochemical synthesis route due to its metastable nature.[29,31] Considering that M90 has a similar composition as $LiMnO_2$, it is remarkable that it can directly form into the DRX structure via a solid-state method, indicating the effectiveness of the Li_3NbO_4 as a cation-disordering agent.[13,43] After the solid-state synthesis, we ball-milled the powder to reduce the particle size, and the XRD peaks become broader, representative of the particle-size reduction. The XRD refinement suggests that the lattice parameter of M90 slightly decreases from 4.1656(7) to 4.1569(2) Å after ball milling (Figure S1, Supporting Information). Scanning electron microscopy (SEM) images show that the as-made M90 forms into big particles (3 µm < d < 20 µm), yet ball-milling pulverizes them into polycrystalline nanoparticles (50 nm < d < 150 nm) that form loosely packed secondary particles (Figure 1c and Figure S2: Supporting Information). Such nanostructured particles have been repeatedly utilized in the literature as it improves the capacity of the DRX cathodes.[10–30] Energy-dispersive-spectroscopy (EDS) mapping shows uniform distribution of Mn, Nb, and O within an M90 particle (Figure 1d), confirming that Nb is soluble in the Mn-rich DRX-oxide lattice. M60 also crystallizes into the DRX-structure, and nanoparticles (80 nm < d < 150 nm) were formed after ball milling (Figures S3 and S4, Supporting Information). The electronic conductivities of the as-made M90 and M60 were measured to be ≈1.8 × 10^{-4} and ≈8.6 × 10^{-5} S cm^{-1}, respectively.

2.2. Electrochemical Properties of M90 and M60

Figure 2a,b shows the voltage profiles of M90 and M60 when they are cycled between 1.5 and 4.8 V at 40 mA g^{-1} and room temperature. We also show their 100 mA g^{-1}-rate voltage profiles in Figure S5 (Supporting Information). We tested the ball-milled samples because the as-made particles (3 µm < d < 20 µm) are too big for the materials to achieve high capacity.[13,27] To the best of our knowledge, no micrometer-size DRX-cathode particles have ever been successfully cycled. While 5%-Li-excess is below the 0-TM percolation threshold (≈10% Li-excess) in the DRX structure, M90 can still deliver an impressively high capacity of ≈250 mAh g^{-1} (≈0.87 Li/f.u.; ≈730 Wh kg^{-1}) with a high 1st-cycle coulombic efficiency of 98.5% through the Li-intercalation reaction (Figure 2a and Figure S6: Supporting Information). Note that although 5%-Li-excess is insufficient for the 0-TM percolation, it is well above the threshold ($x > $ 0.75 in $Li_xTM_{2-x}O_2$) for percolation of mixed 0-TM and 1-TM channels (Figure 1a),[11] suggesting that Li diffusion through mixed 0/1-TM channels could be sufficient to cycle M90. Meanwhile, M60 delivers a slightly higher first-discharge capacity of 277 mAh g^{-1} (≈0.95 Li/f.u.; 860 Wh kg^{-1}); yet, its capacity fades to below 250 mAh g^{-1} after the initial three cycles (Figure 2b). Note that the measured 277 mAh g^{-1} is quite higher than the theoretical Mn-contribution of 175.04 mAh g^{-1} (even if all 0.6 Mn are fully utilized), assuring significant oxygen anion-redox $O^{2-} \leftrightarrow O^-$ contribution in M60. The discharge capacity delivered above 3 V is higher for M60 than M90. This is likely due to more O-redox contribution in M60 than M90 since O^{2-}/O^{1-} is
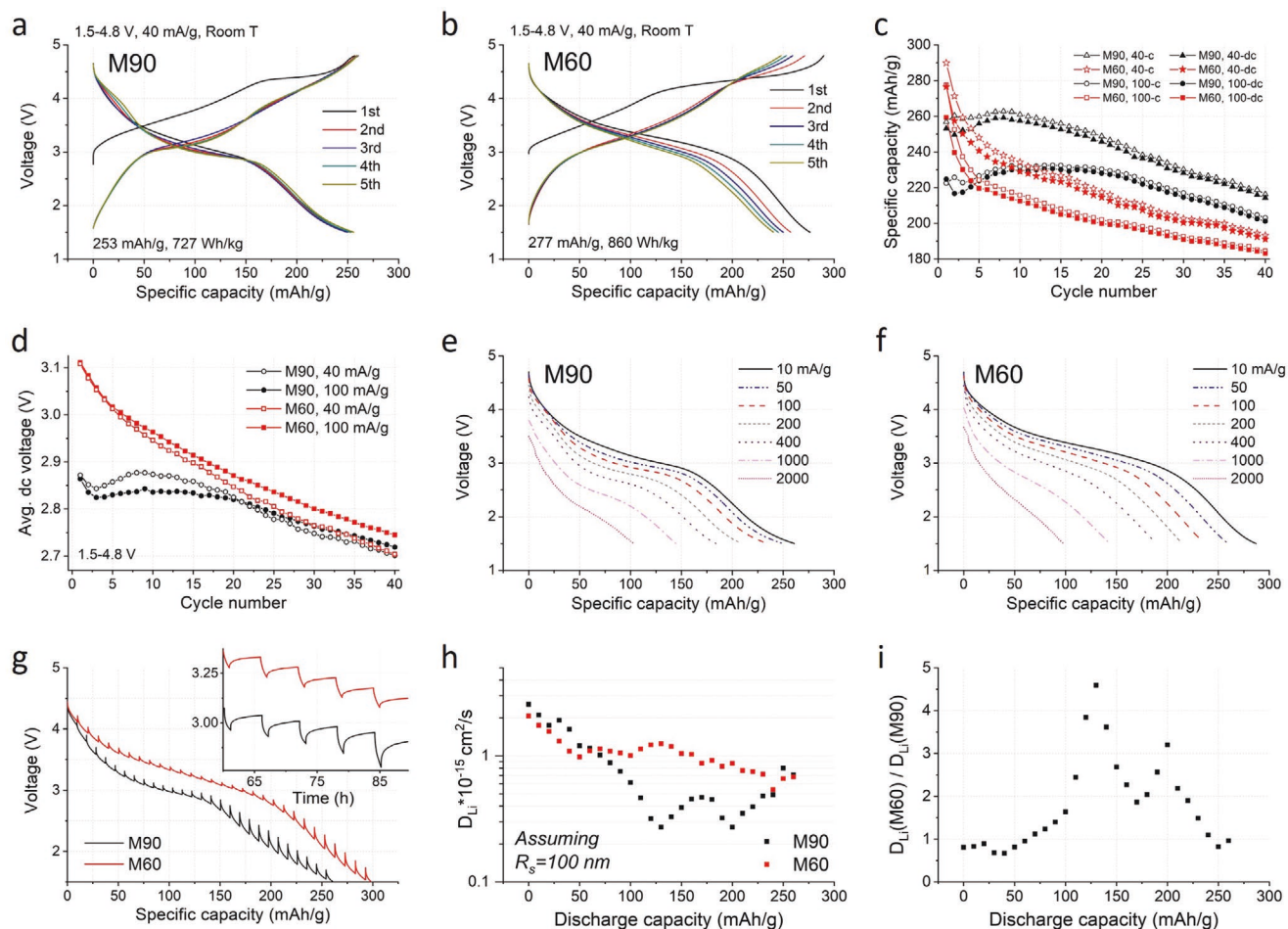
Figure 2. The initial five-cycle voltage profiles of a) M90 and b) M60 when they are cycled at 40 mA g^{-1} between 1.5 and 4.8 V. c) The capacity retention of M90 and M60 during the 40 and 100 mA g^{-1} cycling tests. d) The average discharge voltage of M90 and M60 upon cycling (40 or 100 mA g^{-1}, 1.5–4.8 V). The discharge profiles of e) M90 and f) M60, when they are charged at 20 mA g^{-1} and then discharged at different rates (10, 50, 100, 200, 400, 1000, and 2000 mA g^{-1}). g) The discharge portion of the galvanostatic intermittent titration technique (GITT) profiles of M90 and M60, shown as a function of discharge capacity. The inset zooms in the portion of the M90's GITT profile shown as a function of time (hours). h) The calculated Li-diffusivities of M90 and M60 based on the GITT results and i) their ratio.

intrinsically a higher voltage redox process than Mn^{3+}/Mn^{4+} redox. Over 40 cycles, there is ≈15% and ≈31% capacity loss for M90 and M60, respectively, indicating better capacity retention for M90 (Figure 2c). Also, the average discharge voltage decreases by 170 meV (145 meV) for M90 and by 400 meV (366 meV) for M60 after 40 cycles at 40 mA g^{-1} (100 mA g^{-1}). Thus, voltage retention is also better for M90 (Figure 2d). It has been shown in the literature that the cycling stability of DRX cathodes declines with an increasing degree of O-redox, as it triggers GOM-related side reactions (e.g., O loss, electrolyte decomposition).[17,20,23,27] Therefore, the improved capacity- and voltage-retention of M90 is likely due to its larger Mn-content than M60, leading to higher Mn-redox capacity contribution relative to O-redox for M90, compared to M60. Note we also tested Li$_{1.10}$Mn$_{0.80}$Nb$_{0.10}$O$_2$ (M80). It delivers a similar capacity (≈255 mAh g^{-1} at 40 mA g^{-1}) as M90 (Figure S7, Supporting Information).

We find that the rate capability of M90 compares well with M60. Figure 2e,f shows the voltage profiles of M90 and M60, respectively, when they are charged at 20 mA g^{-1} and

discharged at different rates (10, 50, 100, 200, 400, 1000, and 2000 mA g^{-1}). Although M60 delivers a higher discharge capacity (287 mAh g^{-1}) than M90 (261 mAh g^{-1}) at 10 mA g^{-1}, their capacities become similar to each other as the discharge rate increases. For instance, M90 and M60 deliver 185 and 189 mAh g^{-1}, respectively, at 400 mA g^{-1}.

For a more quantitative comparison of the kinetic properties of M90 and M60, we performed the galvanostatic intermittent titration technique (GITT) measurement with a 5 h relaxation step after every charging or discharging increment of 10 mAh g^{-1} (at 20 mA g^{-1}). Figure 2g shows the 1st discharge portion of the GITT profile with the characteristic vertical voltage shifts corresponding to the voltage relaxation (overpotential).[44] Slightly reduced overpotential is observed from M60 compared to M90, indicating improved kinetics in M60. For instance, after the first discharging to 150 mAh g^{-1}, voltage relaxation is ≈44 meV for M60, while it is ≈166 meV for M90. The estimation of the chemical Li diffusion coefficient based on the GITT profiles suggests about 1.2–5.0 times higher apparent diffusivity for M60 than M90 during discharge,

**ADVANCED
SCIENCE NEWS**

www.advancedsciencenews.com

**ADVANCED
ENERGY
MATERIALS**

www.advenergymat.de

while the absolute magnitudes for both compounds are at the low range of 10^{-16} to 10^{-15} cm^2 s^{-1} (Figure 2h,i and Figure S8: Supporting Information). As a comparative reference, the chemical Li diffusion coefficient of layered LiCoO$_2$ is between 10^{-13}–10^{-11}cm^2 s^{-1}.[45] Note that diffusivity calculation on pulverized cathode particles tends not to be precise because of the irregular particle morphology, while the mathematical model used to fit the GITT profile requires certain assumptions about the geometry of the electrode or electrode particles (Figure S8, Supporting Information). However, considering that both M90 and M60 were synthesized and processed to have similar morphology, the diffusivity ratio between the two materials would still be meaningful (Figure 2i). Considering all, we confirm that Li-excess indeed improves Li-transport in the DRX structure. However, the degree of improvement from 0/1-TM percolation to 0-TM percolation is by less than one order of magnitude, and the Li-diffusivity remains low for both compounds.

Note that the 0-TM percolation concept relates to the intrinsic Li diffusivity rather than the chemical diffusion coefficient that contains the thermodynamic factor.[10,11,23] However, knowing that chemical diffusion is the process that occurs in the presence of concentration (or chemical potential) gradient, resulting in a net transport of mass (thus reflecting the net Li transport in and out of the cathode), we believe that the estimation of the chemical Li diffusivity is useful to evaluate the practical impact of 0-TM percolation. At this point, we have no clear explanation about why the improvement in the chemical diffusivity is not significant after 20% Li-excess. It might be due to the formation of short-range order (SRO) in M60, which can degrade the quality of 0-TM percolation compared to when the cation distribution is completely random.[23] Or, M90, as a highly Mn-rich oxide, may experience local DRX-to-spinel transformation during cycling, which could improve its Li-transport property compared to when M90's structure remains fully cation-disordered.[11,29] Hidden structural parameters such as these can make the diffusivity improvement via Li-excess less evident in the Mn-DRX. Meanwhile, our XRD refinement indicates that the degree of spinel transformation in the first-cycled M90 should not be significant enough (<14% spinel-character developed at maximum) for it to modify the percolation property meaningfully (Figure S9, Supporting Information).[11] Thus, we believe the good performance of M90 achievable from the beginning of cycling should be discussed in the context of conventional DRX materials, although the positive influence on Li transport by the spinel formation cannot be neglected completely.

On the other hand, while the Li-diffusivity may be low for both M90 and M60, the materials' reversible capacity and rate performance are still quite good, indicating that Li-diffusion is not the major bottleneck when the particle size is sufficiently small. This observation is not surprising considering that in a spherical nanoparticle, for example, with $d = 100$ nm, only 20 nm diffusion length is necessary to access $\approx$80% of the capacity. This translates to a minimum of only $\approx$2 $\times$ 10^{-15} cm^2 s^{-1} ($\approx$5 $\times$ 10^{-17} cm^2 s^{-1}) for a 30 min (20 h) charge or discharge (according to the relationship of $x^2 \sim Dt$) (Figure S10, Supporting Information). Furthermore, we observe that for this reduced particle size, a pseudocapacitive rather than diffusion-limited signature emerges in the cyclic voltammetry profiles of M90 or M60 (Figure S11, Supporting Information).

2.3. Chemistry-Dependent Effects of Li-Excess on the DRX-Capacity

Turning to the DRX-cathode literature, we note that nearly all previous studies utilized $d < 200$ nm nanoparticles either directly (e.g., sol–gel, mechanochemistry) or by "post-synthesis" pulverization (as we did for M90 and M60). As motivated above, the difference between 0-TM percolation and mixed 0-TM/1-TM percolation with respect to the characteristic diffusion time should not be significant at small particle length scales. Nevertheless, for certain DRX-cathode chemistries, there is a clear positive correlation between the degree of Li-excess and achieving high capacity. As shown in **Figure 3**a, nominally stoichiometric DRX-LiFeO$_2$, LiCoO$_2$, and LiNiO$_2$ (compounds 1, 9, and 10 in Figure 3a) can discharge <$\approx$50 mAh g^{-1} even when heavily pulverized,[15,31] but the highly Li-excess versions, such as Li$_{1.2}$Ni$_{1/3}$Ti$_{1/3}$Mo$_{2/15}$O$_2$ and Li$_{1.24}$Fe$_{0.38}$Ti$_{0.38}$O$_2$, (compounds 15, 19, respectively) can deliver a high capacity of over 200 mAh g^{-1}, due to reduced voltage of oxygen-redox as well as being assisted by 0-TM percolation (see later discussion).[16,25] To provide additional context to our results, included in Figure 3a are also discharge capacities of several other DRX-cathodes reported in the literature obtained under a slow rate (e.g., 20 mA g^{-1}) (Figure 3a).

To reconcile the inconsistency that Li-excess strongly correlates with the achieved capacity in some cases but not in others (depicted in Figure 3a), we consider two factors that can curtail the reversible capacity. One possibility (case 1) is the slow kinetics contribute excessive over-potential during charge preceding discharge, and the voltage cut-off is prematurely reached before appreciable capacity can be accrued. This explanation is consistent with the percolation theory framework of Li-excess, which is a kinetic argument that 0-TM percolation is a prerequisite for high capacity.[10,11]

Another possibility (case 2) is limited charging capability due to the high thermodynamic redox potential of a cathode. For instance, Li$_2$MnP$_2$O$_7$ shows limited capacity because the equilibrium redox potential to cycle the second Li is too high (5.3 V).[46] Moreover, materials with high redox potential have disadvantages regarding charging; because, for them, there will be less room to apply overpotential before the predetermined charge cut-off (e.g., 4.8 V, which is often limited by the electrolyte electrochemical stability) is reached, rendering slow kinetics less acceptable. In principle, the charging capacity could continuously increase to its maximum by applying higher and higher voltage, but this would require the development of electrolytes with ultra-high stability. Also, Li-TM-oxides typically have poor structural stability at high voltage, experiencing irreversible cation migration and O loss. Thus, there is a practical upper-voltage limit to which a cathode can accumulate the charge capacity ($\leq$4.8 V in lab tests) to ensure enough room for discharge. These explanations then suggest that the cathode's redox potential (a thermodynamic property), which extends to the choice of TM and crystal structure, can further influence the accessible capacity of the cathode.

Investigating case 2 further as a limiting factor for DRX-materials, we plot the reported capacities of DRX-cathodes for a fixed degree of Li-excess (0%) organized by TM in Figure 3b and remark that "not all" 0%-Li-excess DRX cathodes perform
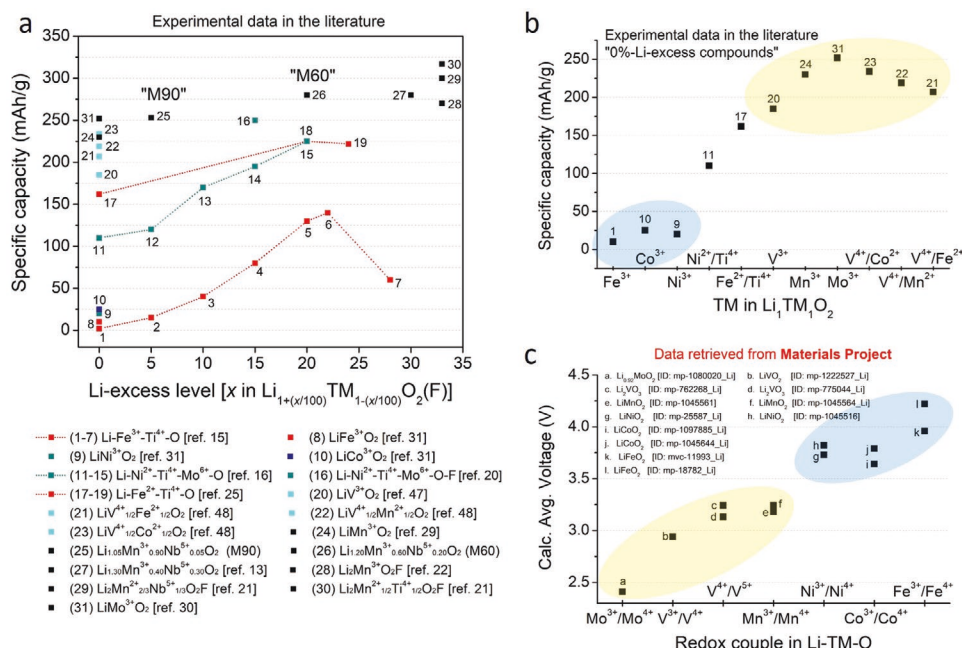
Figure 3. a) The reported capacities of various DRX cathodes as a function of the Li-excess level. b) The specific capacity of the 0%-Li-excess DRX compounds, shown as a function of the TM-species in the crystal structure. c) The calculated average voltage of various Li-TM oxide compounds (note that they are not the DRX compounds) as a function of the redox couple in the compounds. These data were retrieved from the Materials Project database.[49]

poorly. For instance, while DRX-LiFeO$_2$, LiCoO$_2$, and LiNiO$_2$ showed limited capacity (<50 mAh g^{-1}),[31,32] DRX-LiVO$_2$, LiV$_{0.5}$Co$_{0.2}$O$_2$, LiMnO$_2$, and LiMoO$_2$ could still deliver high capacity (≈200 mAh g^{-1}).[29,30,47,48] This suggests that the achievable capacity indeed does not depend entirely on the cycling kinetics, which is expected to be slow in all 0% Li-excess DRXs. To identify a possible correlation between the discharge capacity values with TM-redox voltage, we also plot in Figure 3c the calculated average voltage of various Li-TM oxides utilizing different TM-redox couples as extracted from the Materials Project database.[49] While the voltages depicted in Figure 3c do not correspond to DRX structures (rather ordered structures such as R-$3m$ LiCoO$_2$ and Imma-LiCoO$_2$), the plot clearly reveals broad trends that exist within oxides. For example, some TM-redox couples (e.g., Ni^{3+}/Ni^{4+}, Fe^{3+}/Fe^{4+}) have categorically higher operating potentials than others (e.g., Mo^{3+}/Mo^{4+}, V^{3+}/V^{4+}, Mn^{3+}/Mn^{4+}). Taking Figure 3b,c together, 0%-Li-excess DRX cathodes with low reversible capacity occur with high-voltage TM-redox couples (e.g., Ni^{3+}/Ni^{4+}), while high capacity is achievable using low-voltage TM-redox couples (e.g., Mo^{3+}/Mo^{4+}). It is therefore critical to take the redox potential into account to understand the achievable capacity of DRX-cathodes.

The combination of high-voltage TM-redox and DRX cathodes presents a multifaceted challenge. As discussed above, materials with high redox potential are more susceptible to overpotential-induced premature-reach of upper cut-off voltage upon charging, so slow kinetics tends to curtail the accumulated charge capacity preceding discharge to greater effect. Moreover, there are inherent, non-diffusion-related problems of the DRX-structure, which aggravate voltage swing and penalize TM oxidation, making charging through high-voltage

TM-oxidation challenging. For instance, it was shown that Ni^{3+}/Ni^{4+}-oxidation barely occurs in the DRX oxides (e.g., Li$_{1.2}$Ni$_{1/3}$Ti$_{1/3}$Mo$_{2/15}$O$_2$, even Ni^{2+}/Ni^{3+}-reservoir is not fully utilized) when it readily occurs in Ni-based layered cathodes (e.g., LiNi$_{1/2}$Mn$_{1/2}$O$_2$).[9,16,20,50] To pinpoint the mechanistic origin, we compare critical differences in the electronic structure and intercalation thermodynamics of DRX and layered cathode materials.

2.4. Promoted TM-Oxidation in Layered Structure Facilitates Charging of Layered Cathodes

In layered structure,[5] the band center positions ($\overline{\varepsilon}$) have the following order: $\overline{\varepsilon}$ (Mn$^{3+/4+}$) > $\overline{\varepsilon}$ (Ni$^{2+/3+}$) > $\overline{\varepsilon}$ (Ni$^{3+/4+}$) > $\overline{\varepsilon}$ (Co$^{3+/4+}$) > $\overline{\varepsilon}$ (O$^{2-/-}$), and Li-extraction using TM-oxidation (e.g., Ni/ Co-oxidation) occurs within a narrow voltage window without much overlap with the O-2p band. For example, nearly ≈80% of Li (≈220 mAh g^{-1}-charge) can be extracted from layered LiNiO$_2$ within 3.5–4.3 V (only 0.8 V voltage swing) via Ni^{3+}/Ni^{4+} oxidation.[31] To explain, we recall that the equilibrium cathode potential (U) is negatively proportional to the chemical potential of Li in the cathode structure ($\mu_{Li}^{cathode} \propto -eU$), which is the sum of the chemical potential of a Li$^+$ ion ($\mu_{Li+}^{cathode}$) and an electron ($\mu_{e-}^{cathode}$).[51] In a layered structure with limited numbers of distinct sites for Li$^+$ ions (e.g., for perfectly layered R-$3m$ LiCoO$_2$, there is only one crystallographically unique site for Li), the Li$^+$-site energy (proportional to $\mu_{Li+}^{cathode}$) varies little upon charging.

Also, in the layered structure, TMs form a distinct TM–O slab (TM-layer, **Figure 4**a), and the TMs can collectively
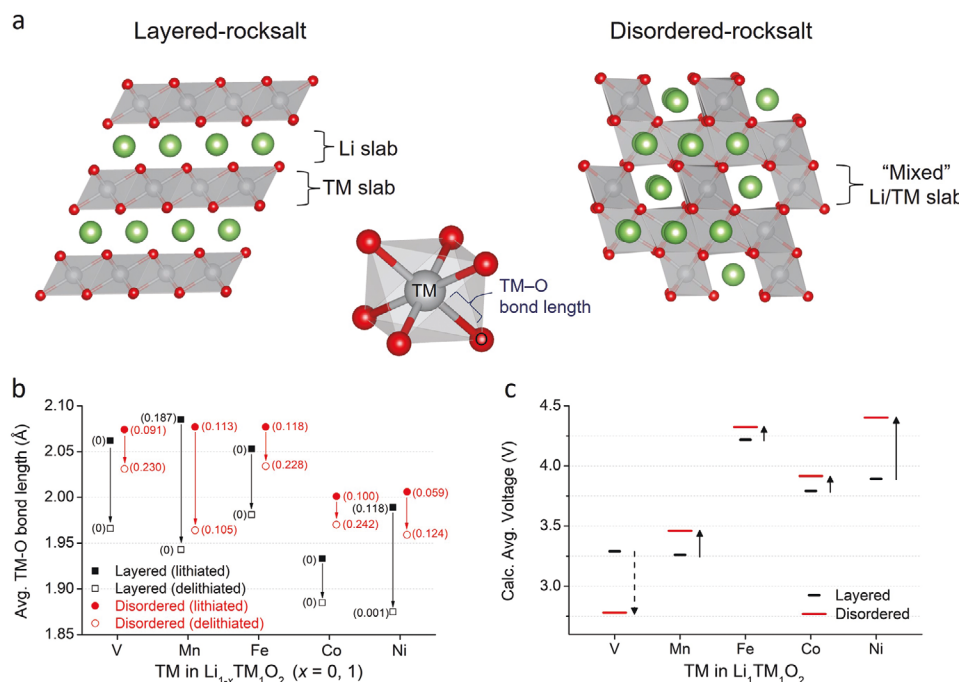
Figure 4. a) The schematics of the layered- and disordered-rocksalt (DRX) structures and TM–O octahedron. b) The computed average TM–O bond length in the layered- or DRX-$Li_{1-x}TM_1O_2$ (TM = V, Mn, Fe, Co, Ni) before ($x = 0$) and after delithiation ($x = 1$): The standard deviations are shown in parentheses. c) The computed average voltage of the layered- or DRX-$Li_{1-x}TM_1O_2$ (TM = V, Mn, Fe, Co, Ni).

reduce their TM–O bond-length upon charge. For instance, it was shown experimentally that the TM–O bond distance of $LiNi_{0.8}Mn_{0.1}Co_{0.1}O_2$ decreases from 1.961 to 1.896 Å when charged to 4.3 V.[52] This trend is also observed in our DFT calculations. Figure 4b shows the change in the average TM–O bond distance in layered $Li_{1-x}TMO_2$ (TM = V, Mn, Fe, Co, Ni) before ($x = 0$) and after delithiation ($x = 1$), predicted by the calculations. The details of this modeling are shown in the Method section. There is a significant decrease in the average TM–O bond length after delithiation in all cases. For instance, the average Ni–O distance is calculated as 1.989 Å (standard deviation, STD: 0.118 Å) in layered $LiNiO_2$, and it decreases to 1.875 Å (STD: 0.001 Å) after Li-removal. This shortened bond length increases the covalency of the TM–O bond through the greater overlap between TM-d and O-2p orbitals in the layered structure, which in turn raises the energy level of the antibonding TM-d-states (e.g., Ni-e_g^*), as demonstrated by Aydinol et al.[51,53] This "upshifted" TM-redox-band (i.e., nonrigid-band effect) facilitates further TM-oxidation upon charging, as it makes further electron-extraction from the band require less energy compared to a rigid band. Moreover, this nonrigid-band effect partially opposes the downshift of the Fermi level upon electron depletion, overall minimizing the variation of $\mu_{e-}^{cathode}$ during charging.[51] With the reduced variation of both $\mu_{Li+}^{cathode}$ and $\mu_{e-}^{cathode}$ and the promoted TM-oxidation by TM–O bond-shortening (ionic relaxation), a large amount of Li can be extracted from layered cathodes at a reasonable voltage with minimal voltage swing. Combining these thermodynamic benefits with fast Li diffusion in the layered structure, high charging capacity through high-voltage TM redox is possible.

2.5. Structurally Limited TM-Oxidation in the DRX Cathodes

However, going from the layered to the DRX structure develops a situation where, in addition to slower Li diffusion imposing greater overpotential, larger voltage-swing, and broadened/deepened TM-d-bands penalize deep cationic charging of DRX-cathodes. First of all, nearly random cation distribution in DRX structure generates various local environments for cations and anions, thus broadening the distribution of both Li+-site energies and TM/O-redox-levels. As a result, the variation of $\mu_{Li+}^{cathode}$ and $\mu_{e-}^{cathode}$ with state of charge is greater in the DRX structure than in the layered structure, which leads to a more sloped voltage profile as widely seen experimentally[13,16,21] and supported theoretically by Abdellahi et al.[54] A large voltage slope pushes the extraction of some electrons to an exceedingly high voltage and thus penalizes achieving high charging capacity.

Furthermore, our DFT calculations find a longer average TM–O bond length in DRX $Li_{1-x}TMO_2$ (TM = V, Mn, Fe, Co, Ni) than in layered $Li_{1-x}TMO_2$ before and after Li-removal, except for (lithiated, $x = 0$) $LiMnO_2$ (Figure 4b). This trend can be explained by the "pillar effect" of large-size Li+ ions ($r = 0.76$ Å) sharing the same cation-slab with smaller-size TM ions (e.g., Co^{3+}: $r = 0.545$ Å) in the DRX structure, resulting in distortion and expansion of the TM–O octahedron. For instance, the average Co–O bond length in DRX $LiCoO_2$ is calculated to be 2.001 Å (STD: 0.1 Å), which is longer than the value (1.933 Å, STD: 0 Å) in layered $LiCoO_2$. This bond elongation makes the bond more ionic, lowering the energy level of TM-d states with an anti-bonding characteristic (e.g., Ni-e_g^*).[51] Also,

ADVANCED
SCIENCE NEWS
www.advancedsciencenews.com

ADVANCED
ENERGY
MATERIALS
www.advenergymat.de

we find a smaller reduction in the TM–O bond length after Li-removal in the DRX structure, showing that the relaxation of the TM–O bond is more limited, rendering the TM-redox band more rigid in the DRX structure than in the layered structure. All these effects would widen the TM cationic-redox bandwidth and make deep TM-oxidation harder in the DRX structure. As a result, our calculations find increased average redox potential for DRX LiMnO$_2$, LiFeO$_2$, LiCoO$_2$, and LiNiO$_2$ than for their layered counterparts (Figure 4c). In particular, consistent with the prediction made by Abdellahi et al.,[54] as high as 4.4 V-average redox potential is predicted for DRX LiNiO$_2$ (vs 3.9 V for layered LiNiO$_2$), rendering a large portion of Li in the structure barely accessible with a practical upper cut-off voltage. Indeed, it was seen experimentally that the first-charge capacity of DRX-LiNiO$_2$ is limited to ≈80 mAh g^{-1} (4.3 V-charge), whereas the capacity can reach ≈220 mAh g^{-1} for layered LiNiO$_2$ (4.3 V-charge).[31] Also, it is known that Ni is hard to oxidize past Ni$^{\approx 3+}$ in the DRX structure.[16,50] Along with slower Li diffusion in DRX structure imposing large overpotential, these added difficulties related to TM-oxidation explain why charging is harder in the DRX cathodes, especially when they are made with high-voltage TMs with deep d-electrons (e.g., Fe, Co, Ni) whose redox potential is high even in the layered structure.

2.6. Resolving the Redox-Potential Issue in the DRX Structure with Li Excess

We find that this redox-potential issue in high-voltage-TM-containing DRX cathodes can be resolved with Li-excess. Along with introducing 0-TM percolation, Li-excess increases the number of local environments for oxygen where some O-2p-orbitals are left unhybridized with TM-orbitals, the so-called Li–O–Li states.[55,56] The lack of hybridization with TMs makes these O-2p states higher in energy than the bonding O-2p states so that oxygen can more easily participate in a redox process. However, it should be noted that according to the rigid band model of Li-TM oxides, O-oxidation (unaccompanied by structure relaxation) occurring after or mixed with problematic high-voltage TM-oxidation will have little impact on improving the DRX's charging performance. This is because the electron level (negatively proportional to the cathode voltage) of the Li–O–Li states will be just as low as the problematically deep TM-d state, although the Li–O–Li states are higher in energy than the bonding O-2p states.[55]

Nevertheless, as we will show below, what makes charging highly Li-excess materials different is the ability for oxidized oxygen in the lattice to form condensed oxygen species (e.g., O$^{2-}_2$, O$^-_2$, lattice O$_2$). In highly Li-excess materials, fewer TM–O bonds need to be broken to form O–O bonds due to lower TM-content (therefore lower TM-coordination number for oxygen), which allows the charged DRX structure to lower its energy significantly.[57] Overall, this structural relaxation makes Li-extraction energetically favorable at a lower voltage.
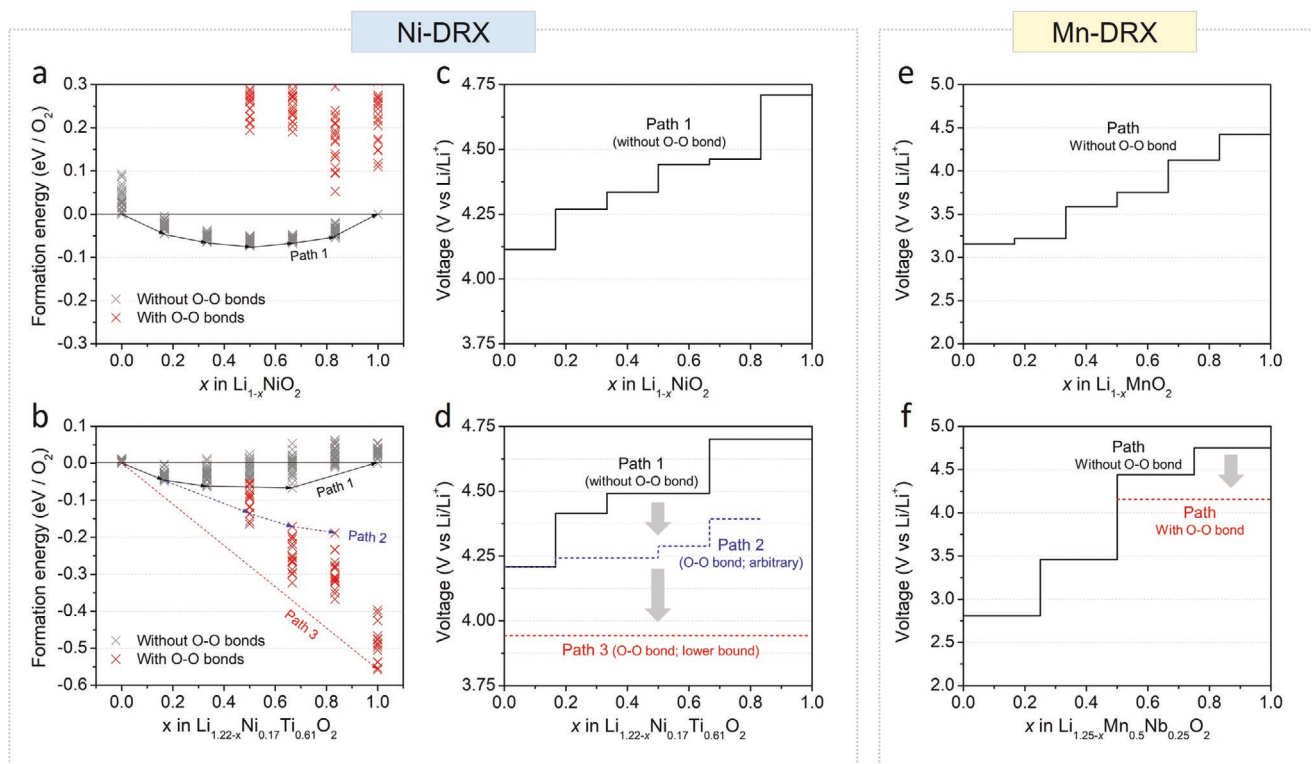
Our DFT calculations confirm this understanding. Figure 5a,b shows the formation energy (eV/O$_2$) of various model DRX Li$_x$NiO$_2$ and Li$_{1.22-x}$Ni$_{0.17}$Ti$_{0.61}$O$_2$ structures as a function of the Li-extraction level (x). Note that due to the

overlap between DRX's deep Ni-redox states (Ni^{3+}/Ni^{4+} for DRX Li$_x$NiO$_2$ and Ni^{2+}/Ni^{4+} for Li$_{1.22-x}$Ni$_{0.17}$Ti$_{0.61}$O$_2$) and O-redox states, we observe concurrent Ni- and O-oxidation not only in Li$_{1.22-x}$Ni$_{0.17}$Ti$_{0.61}$O$_2$ (whose Ni^{2+}/Ni^{4+} reservoir permits only 0.34 Li extraction at maximum, requiring O-oxidation for full Li extraction) but also in Li$_x$NiO$_2$ (whose Ni^{3+}/Ni^{4+}-redox reservoir is large enough to cover full Li-extraction) (Figure S12, Supporting Information). Gray and red data points represent the formation energies of the structures without (black) or with (red) condensed O-species developed upon ab-initio molecular dynamic (AIMD) simulation at 1500 K (see the Experimental Section for details). We observe short O—O bonds with the bond length of ≈1.45 Å (peroxide) or ≈1.29 Å (superoxide) when performing AIMD (at 1500 K) for highly Li-extracted DRX structures (Figure S13, Supporting Information).

Interestingly, for DRX Li$_x$NiO$_2$, the system total energies of the Li-extracted structures with short O–O bonds (developed upon AIMD simulation) are higher than those without the bonds, whereas the opposite case is observed for DRX Li$_{1.22-x}$Ni$_{0.17}$Ti$_{0.61}$O$_2$ (Figure 5a,b). This result suggests that after O-oxidation, Li$_{1.22}$Ni$_{0.17}$Ti$_{0.61}$O$_2$ can lower its energy by forming condensed O-species in its structure, which is not the case for DRX LiNiO$_2$ (note the particle surface of LiNiO$_2$ may develop oxygen dimers due to Ni-under coordination). Also, the O–O bonds in Li$_{1.22-x}$Ni$_{0.17}$Ti$_{0.61}$O$_2$ were made between oxygen ions with low TM-coordination, supporting our understanding that low TM-content in Li-excess materials (resulting in low TM-coordination for O) facilitates the formation of condensed oxygen species (Figure S12, Supporting Information). In turn, this effect decreases the voltage for Li$_{1.22}$Ni$_{0.17}$Ti$_{0.61}$O$_2$ compared to the one without the effect. Note that precise prediction of a DRX material's voltage profile using DFT calculations is challenging due to the difficulties of modeling the complex cation-distribution in the material using a supercell with a limited size. For DRX LiNiO$_2$, the lowest-voltage Li-extraction would not involve the O–O bond formation, leading to the average voltage of ≈4.38 V (Figure 5c). For DRX Li$_{1.22}$Ni$_{0.17}$Ti$_{0.61}$O$_2$ (Figure 5d), Li-extraction voltage can decrease from the average of ≈4.50 V (Path 1, without O–O bonds) to ≈4.28 V (Path 2, an arbitrary path with O–O bonds) and ≈3.94 V (Path 3, the lowest voltage path with O–O bonds) by forming O–O bonds, revealing that high Li-excess triggering O-oxidation and O–O bond formation can substantially facilitate the charging of Ni-DRXs. This result, in turn, suggests that DRX materials with barely oxidizable TMs (e.g., Ni^{3+}, Fe^{3+}, Co^{3+}) can resolve their charging issue via Li-excess, resulting in high charging capacity and room for high discharge capacity (e.g., compounds 1–7 and 11–15 in Figure 3a).[15,16,25]

Meanwhile, the charging voltage is predicted to be reasonable for both DRX LiMnO$_2$ (≈3.71 V average, O–O bonds are not favored) and Li$_{1.25}$Mn$_{0.5}$Nb$_{0.25}$O$_2$ (≈3.86 V average without O–O bond; ≈3.65 V with O–O bond) (Figure 5e,f and Figure S13: Supporting Information), explaining how DRX-cathodes with low-voltage TMs (e.g., V, Mo, Mn) could achieve high charging (reversible) capacity regardless of Li-excess (Figure 3b).[29,30,47,48] In this case, the benefit of Li-excess would remain at the diffusivity-improvement-level (0-TM percolation), which becomes less important once the particle size is sufficiently reduced.

ADVANCED
SCIENCE NEWS
www.advancedsciencenews.com

ADVANCED
ENERGY
MATERIALS
www.advenergymat.de

Figure 5. a,b) The DFT formation energies (eV/O$_2$) of various a) DRX Li$_{1-x}$NiO$_2$ and b) Li$_{1.22-x}$Ni$_{0.17}$Ti$_{0.61}$O$_2$ model structures as a function of the Li-extraction level (*x*). The gray and red points represent the energies of the structures without and with the short O−O bonds (formed upon AIMD simulation at 1500 K), respectively. Path 1 in the Figure corresponds to Li-extraction, which would not lead to the O−O bond formation. Paths 2 (arbitrary) and Path 3 (the lowest voltage path) in Figure 5b involve O−O bond formation upon O-oxidation. c,d) The DFT voltage profiles of c) DRX LiNiO$_2$ and d) Li$_{1.22}$Ni$_{0.17}$Ti$_{0.61}$O$_2$ constructed based on different paths. e,f) The DFT voltage profile of e) DRX LiMnO$_2$ and f) Li$_{1.25}$Mn$_{0.5}$Nb$_{0.25}$O$_2$. For Li$_{1.25}$Mn$_{0.5}$Nb$_{0.25}$O$_2$, voltage profiles taking two different paths were shown as the O−O bond formation can decrease its voltage while it is not for DRX LiMnO$_2$.

2.7. Dual Roles of Li-Excess in DRX Cathodes

To summarize, Li-excess (*x* > 0 in Li$_{1+x}$TM$_{1-x}$O$_2$) plays at least two roles in DRX cathodes. Increasing *x* enhances Li bulk diffusion via 0-TM percolation,[10,11,23] but this should become less critical with reduced transport length in small particles. Our finding that Li$_{1.05}$Mn$_{0.90}$Nb$_{0.05}$O$_2$ (M90) with sufficiently small particle size demonstrates high capacity comparable with a much higher Li-excess version (M60) serves as confirmation. The notion of Mn-based DRX materials being able to operate without a high degree of Li-excess is interesting because nearly all previous reports on Mn-DRXs describe synthesis with both high degrees of Li-excess (to ensure 0-TM percolation) and pulverization into small polycrystalline nanoparticles (*d* < 200 nm).[13,14,21,24,28] Moreover, mechanochemically synthesized Mn-based DRX cathodes (e.g., Li$_2$Mn$_{2/3}$Nb$_{1/3}$O$_2$F) typically have 10–20 nm nano-grains in each primary particle,[21,22] which should further render high Li-diffusivity non-critical given such a short diffusion length.

While apparently uncritical for certain chemistries, introducing significant Li-excess is necessary to enable high capacity in DRX cathodes comprised of high-voltage TMs (e.g., Fe^{3+}, Co^{3+}, Ni$^{2+,3+}$). It is important to note that Ni^{2+}/Ni^{3+}/Ni^{4+} and Co^{3+}/Co^{4+} redox are accessible at a reasonable voltage in layered materials but not in the DRX materials. In this case, introducing Li-excess offsets TM-oxidation with O-oxidation accompanied by short O−O bond formation, which enables significant Li-extraction at a lower, more reasonable voltage (4.3–4.6 V), leaving room for discharge. On the other hand, low-voltage TMs (e.g., Mn^{3+}, Mo^{3+}, V^3) are readily oxidizable in the DRX structure. Thus, the low-voltage TM-DRXs do not require a high degree of Li-excess to operate once their particle size is sufficiently reduced, as shown in Figure 3b. So while DRX cathodes with high-voltage TMs and low-voltage TMs are both capable of high capacity, the former must rely on O-redox with Li-excess, and the latter can utilize TM-redox without significant Li-excess. In other words, in order to achieve >200 mAh g^{-1}, Ni/Co/Fe-DRX has to be more HACR, relying more heavily on Li-excess, whereas Mn/Mo/V-DRX can work well with more conventional TM-redox with light (or without) Li-excess as long as the particle size is nanoscale.

Ultimately, capacity from TM-redox can be regarded as a "safe asset" compared to O-redox (a "risky asset"), which triggers O-loss and permanent structural damage by promoting global oxygen mobility (GOM).[5] Fortunately, the Li-excess constraint is effectively removed in low-voltage-TM (V/Mn/Mo)-based DRXs to increase the TM-redox reservoir, minimizing the risk of detrimental O-redox-related side-reactions.[20,36,37,39] As a further downstream consequence, with more Mn or other TMs replacing Li, the electronic conductivity could reasonably increase, allowing for higher active material content and reduced

carbon content in the cathode film, leading to higher cell-level energy density. Overall, great attention must be devoted to identifying "Goldilocks" Li-excess levels, such that the improved beginning-of-life capacity via Li-excess does not rapidly fade upon extended cycling due to excessive GOM-side reactions.

It is worth noting that the near entirety of the DRX literature, including this work, has focused primarily on small particle sizes so that low intrinsic Li diffusivity can be acceptable. However, regardless of the particle size, high Li diffusivity is beneficial for both capacity and rate performance. Moreover, in practice, large particles are desirable for improved cathode packing density, reduced side reactions with the electrolyte, less TM-dissolution (e.g., Mn-dissolution from Mn-DRX), and surface treatments for enhanced cycling stability.[58,59] To cycle large particles, intrinsic Li-diffusivity must be sufficiently high to support long-range Li-diffusion at a reasonable rate. Therefore, we believe that 0-TM percolation enabled by Li-excess will continue to play an important role in the design of the DRX cathodes, and detailed studies on the SRO effect on the percolation or the role of the thermodynamic factor on the chemical Li diffusivity must be conducted to optimize the 0-TM percolation for the fastest Li-transport.[23,60,61]

Finally, most DRX researches, including this work, have used a large amount of conductive carbon (usually 20–30 wt%) in the electrode film to minimize the impact of DRX's electronic conductivity on their performance.[10–30] However, a practical electrode should contain a minimum amount of carbon (<5 wt%) for high energy density,[58] for which the electronic conductivity of the DRX particles itself should be sufficiently high. In this context, we believe the systematic study of the electronic conductivity, likely influenced by both the Li-excess level and TM chemistry, must be followed in future DRX research.

3. Conclusion

In this work, based on the experimental results of high capacity (>250 mAh g^{-1}) in both $Li_{1.05}Mn_{0.90}Nb_{0.05}O_2$ and $Li_{1.20}Mn_{0.60}Nb_{0.20}O_2$, exhaustive literature examination, and supporting DFT calculations, we demonstrated that "Li-excess" – widely considered essential to unlock the capacity of the DRX cathodes by enabling bulk Li diffusion – is non-critical for low-voltage TM-based DRXs at the nanoparticle scale. Meanwhile, regardless of the particle size, Li-excess is crucial for DRXs made with high-voltage TMs (e.g., Ni), as it lowers the charging voltage of those cathodes (through the formation of condensed oxygen species upon oxygen oxidation), which otherwise would face difficulties in charging due to their excessively high redox potential. This understanding, in turn, suggests that the Li-excess can be cut back to maximize the TM-redox capacity and reduce the O-redox activity for the low-voltage TM DRXs to improve their cycling stability, which has been a significant bottleneck for their practical use in Li-ion batteries.

4. Experimental Section

Material Synthesis: To synthesize $Li_{1.05}Mn_{0.90}Nb_{0.05}O_2$ (M90) and $Li_{1.20}Mn_{0.60}Nb_{0.20}O_2$ (M60), Li_2CO_3 (Alfa Aesar, ACS, 99% min), Mn_2O_3 (Alfa Aesar, 98%), and Nb_2O_5 (Alfa Aesar, 99.5%) were used as precursors. The stoichiometric amount of Mn_2O_3 and Nb_2O_5 needed to form the compounds were mixed with a 10% excess amount of Li_2CO_3 precursors through the planetary ball-mill (PQ-N2, Across International) for 6 h at 400 rpm: the excess amount of Li_2CO_3 was to compensate for the possible loss of lithium during the calcination. Then, the precursor mixture was pelletized and calcined for 1 h in Argon at 1300 °C for M90 and 1100 °C for M60, followed by furnace cooling to room temperature: the ramping rate was 5 °C min^{-1} (≈4 h to reach 1300 or 1100 °C). After the calcination, the pellets were manually ground into fine powders. Then, the as-made M90 and M60 powders were planetary-ball-milled (MSK-PCV-300, MTI) into nanoparticles under the vacuum condition. The 3 g of powders were put in a 30 mL Cr12MoV steel container with 25 g of zirconia balls. Then, two-rounds of 1000 rpm (for 3 min)–600 rpm (for 3 min)–1000 rpm (for 3 min) ball mill was conducted, and there was a 20 min rest between the rounds to prevent overheating. After the ball mill, the pulverized powders were manually collected and stored in an Argon-filled glovebox.

Electrochemical Tests: To prepare a cathode film, first 350 mg of the pulverized M90/M60 and 100 mg of carbon black (TIMCAL, Super C65) was mixed by ball-milling (MSK-PCV-300, MTI) for 3 min at 600 rpm. Then, 180 mg of the mixture powder and 20 mg of polytetrafluoroethylene (PTFE, DuPont, Teflon 8 A) were manually mixed using a mortar and pestle and rolled into a thin film in an Ar-filled glovebox, such that the weight ratio between the active material, carbon black, and PTFE becomes 70:20:10 in the film. Coin cells (CR2032) were assembled with the cathode, the Li-counter electrode, a glass-fiber separator (Whatman), and a 1 M solution of $LiPF_6$ in a mixture of ethyl carbonate/dimethyl carbonate (EC/DMC, 1:1 v/v) in an Ar-filled glove box. The active material's loading on the cathode film was ≈4 mg cm^{-2}. The galvanostatic charge/discharge, intermittent titration tests, and rate-capability tests were performed using a potentiostat (LAND CT2001, China) at room temperature otherwise specified. The specific capacity was calculated based on the amount of the active material in the cathode film. The cyclic voltammetry test was conducted using the Gamry reference 3000. The scan-rate was sequentially increased from 0.1 to 0.2 mV s^{-1}, 0.5 mV s^{-1}, 0.7 to 1 mV s^{-1}, upon the anodic sweep to 4.8 V and cathodic sweep to 1.5 V.

Material Characterization: The X-ray diffraction (XRD) patterns were collected on a PANalytical multipurpose diffractometer (Cu source) in the 2Θ range of 15°–85°. To perform XRD on the cycled electrodes, coin cells were dissembled in an Ar-filled glovebox and washed with dimethyl carbonate (DMC). Then, the cathode film was sealed with Prolene thin-film (Chemplex Spectromembrane 3018) and vacuum grease and was placed on a zero-background silicon holder. The Rietveld refinement on the collected XRD patterns was completed using the PANalytical X'pert HighScore Plus software. Scanning electron microscopy (SEM) and energy-dispersive-X-ray spectroscopy were performed with the Zeiss Merlin High-resolution SEM. Elemental analysis of the compounds was performed with (ICP-OES, Agilent 725 ICP-OES) for lithium, manganese, and niobium. To measure the electrical conductivity, first the as-made M90 or M60 powder was pressed into a pellet under a pressure of 12 tons for 5 min. The pellet diameter was 11 mm. Both M90 and M60 pellets had a thickness of ≈0.05 mm, measured by a Vernier caliper. The electrical conductivities of the samples were measured by a Four Point Probe Resistive machine (RST-9 from 4 Probes Tech).

DFT Calculations: All calculations were performed using density functional theory (DFT) as implemented in the Vienna ab initio simulation package.[62] The Perdew–Burke–Ernzerhof functional[63] was adopted for spin-polarized generalized gradient approximation (GGA) calculations. Hubbard U correction (GGA+U) was introduced for all TM atoms except Ti and Nb to compensate for the self-interaction error of GGA.[64] U values were 3.2, 3.9, 5.3, 3.3, and 6.2 eV for V, Mn, Fe, Co, and Ni, respectively.[49] Projector augmented wave potentials were employed with kinetic energy cut-off of 520 eV and k-point meshes with their densities of at least 1000 per number of atoms in the supercell. All structures were fully relaxed until the forces on atom converged within 0.05 eV. The method to prepare the structures by AIMD is provided in the Supporting Information.

Supporting Information

Supporting Information is available from the Wiley Online Library or from the author.

Conflict of Interest

The authors declare no conflict of interest.

Data Availability Statement

The data that support the findings of this study are available from the corresponding authors upon reasonable request.

[1] M. S. Whittingham, *Chem. Rev.* **2004**, *104*, 4271.
[2] E. A. Olivetti, G. Ceder, G. G. Gaustad, X. Fu, *Joule* **2017**, *1*, 229.
[3] W. Xue, Z. Shi, L. Suo, C. Wang, Z. Wang, H. Wang, K. P. So, A. Maurano, D. Yu, Y. Chen, Q. Long, Z. Zhu, G. Xu, J. Kong, J. Li, *Nat. Energy* **2019**, *4*, 374.
[4] M. Sathiya, G. Rousse, K. Ramesha, C. P. Laisa, H. Vezin, M. T. Sougrati, M. L. Doublet, D. Foix, D. Gonbeau, W. Walker, A. S. Prakash, M. Ben Hassine, L. Dupont, J. M. Tarascon, *Nat. Mater.* **2013**, *12*, 827.
[5] Z. Zhu, D. Yu, Y. Yang, C. Su, Y. Huang, Y. Dong, I. Waluyo, B. Wang, A. Hunt, X. Yao, J. Lee, W. Xue, J. Li, *Nat. Energy* **2019**, *4*, 1049.
[6] K. Turcheniuk, D. Bondarev, V. Singhal, G. Yushin, *Nature* **2018**, *559*, 467.
[7] Z. Lu, D. D. MacNeil, J. R. Dahn, *Electrochem. Solid-State Lett.* **2001**, *4*, A200.
[8] M. M. Thackeray, S.-H. Kang, C. S. Johnson, J. T. Vaughey, R. Benedek, S. A. Hackney, *J. Mater. Chem.* **2007**, *17*, 3112.
[9] S. Hy, H. Liu, M. Zhang, D. Qian, B.-J. Hwang, Y. S. Meng, *Energy Environ. Sci.* **2016**, *9*, 1931.
[10] J. Lee, A. Urban, X. Li, D. Su, G. Hautier, G. Ceder, *Science* **2014**, *343*, 519.
[11] A. Urban, J. Lee, G. Ceder, *Adv. Energy Mater.* **2014**, *4*, 1400478.
[12] A. Sakuda, T. Takeuchi, K. Okamura, H. Kobayashi, H. Sakaebe, K. Tatsumi, Z. Ogumi, *Sci. Rep.* **2015**, *4*, 4833.
[13] N. Yabuuchi, M. Takeuchi, M. Nakayama, H. Shiiba, M. Ogawa, K. Nakayama, T. Ohta, D. Endo, T. Ozaki, T. Inamasu, *Proc. Natl. Acad. Sci. USA* **2015**, *112*, 7650.
[14] R. Wang, X. Li, L. Liu, J. Lee, D.-H. Seo, S.-H. Bo, A. Urban, G. Ceder, *Electrochem. Commun.* **2015**, *60*, 70.
[15] S. L. Glazier, J. Li, J. Zhou, T. Bond, J. R. Dahn, *Chem. Mater.* **2015**, *27*, 7751.
[16] J. Lee, D.-H. Seo, M. Balasubramanian, N. Twu, X. Li, G. Ceder, *Energy Environ. Sci.* **2015**, *8*, 3255.
[17] N. Yabuuchi, M. Nakayama, M. Takeuchi, S. Komaba, Y. Hashimoto, T. Mukai, H. Shiiba, K. Sato, Y. Kobayashi, A. Nakao, *Nat. Commun.* **2016**, *7*, 13814.
[18] R. Chen, S. Ren, M. Knapp, D. Wang, R. Witter, M. Fichtner, H. Hahn, *Adv. Energy Mater.* **2015**, *5*, 1401814.
[19] R. Chen, S. Ren, X. Mu, E. Maawad, S. Zander, R. Hempelmann, H. Hahn, *ChemElectroChem* **2016**, *3*, 892.
[20] J. Lee, J. K. Papp, R. J. Clément, S. Sallis, D.-H. Kwon, T. Shi, W. Yang, B. D. McCloskey, G. Ceder, *Nat. Commun.* **2017**, *8*, 981.
[21] J. Lee, D. A. Kitchaev, D.-H. Kwon, C.-W. Lee, J. K. Papp, Y.-S. Liu, Z. Lun, R. J. Clément, T. Shi, B. D. McCloskey, *Nature* **2018**, *556*, 185.
[22] R. A. House, L. Jin, U. Maitra, K. Tsuruta, J. W. Somerville, D. P. Förstermann, F. Massel, L. Duda, M. R. Roberts, P. G. Bruce, *Energy Environ. Sci.* **2018**, *11*, 926.
[23] H. Ji, A. Urban, D. A. Kitchaev, D.-H. Kwon, N. Artrith, C. Ophus, W. Huang, Z. Cai, T. Shi, J. C. Kim, *Nat. Commun.* **2019**, *10*, 592.
[24] E. Zhao, L. He, B. Wang, X. Li, J. Zhang, Y. Wu, J. Chen, S. Zhang, T. Liang, Y. Chen, *Energy Storage Mater..* **2019**, *16*, 354.
[25] M. Yang, J. Jin, Y. Shen, S. Sun, X. Zhao, X. Shen, *ACS Appl. Mater. Interfaces* **2019**, *11*, 44144.
[26] Q. Jacquet, A. Iadecola, M. Saubanère, H. Li, E. J. Berg, G. l. Rousse, J. Cabana, M.-L. Doublet, J.-M. Tarascon, *J. Am. Chem. Soc.* **2019**, *141*, 11452.
[27] W. H. Kan, C. Wei, D. Chen, T. Bo, B. T. Wang, Y. Zhang, Y. Tian, J. S. Lee, Y. Liu, G. Chen, *Adv. Funct. Mater.* **2019**, *29*, 1808294.
[28] D. A. Kitchaev, Z. Lun, W. D. Richards, H. Ji, R. J. Clément, M. Balasubramanian, D.-H. Kwon, K. Dai, J. K. Papp, T. Lei, *Energy Environ. Sci.* **2018**, *11*, 2159.
[29] T. Sato, K. Sato, W. Zhao, Y. Kajiya, N. Yabuuchi, *J. Mater. Chem. A* **2018**, *6*, 13943.
[30] N. Takeda, S. Hoshino, L. Xie, S. Chen, I. Ikeuchi, R. Natsui, K. Nakura, N. Yabuuchi, *J. Power Sources* **2017**, *367*, 122.
[31] M. Obrovac, O. Mao, J. R. Dahn, *Solid State Ionics* **1998**, *112*, 9.
[32] K. Kang, D. Carlier, J. Reed, E. M. Arroyo, G. Ceder, L. Croguennec, C. Delmas, *Chem. Mater.* **2003**, *15*, 4503.
[33] X. Wang, L. Gao, F. Zhou, Z. Zhang, M. Ji, C. Tang, T. Shen, H. Zheng, *J. Cryst. Growth* **2004**, *265*, 220.
[34] W. E. Gent, K. Lim, Y. Liang, Q. Li, T. Barnes, S.-J. Ahn, K. H. Stone, M. McIntire, J. Hong, J. H. Song, *Nat. Commun.* **2017**, *8*, 2091.
[35] K. Dai, J. Wu, Z. Zhuo, Q. Li, S. Sallis, J. Mao, G. Ai, C. Sun, Z. Li, W. E. Gent, *Joule* **2019**, *3*, 518.
[36] E. Hu, X. Yu, R. Lin, X. Bi, J. Lu, S. Bak, K.-W. Nam, H. L. Xin, C. Jaye, D. A. Fischer, *Nat. Energy* **2019**, *3*, 690.
[37] S. Myeong, W. Cho, W. Jin, J. Hwang, M. Yoon, Y. Yoo, G. Nam, H. Jang, J.-G. Han, N.-S. Choi, *Nat. Commun.* **2018**, *9*, 3285.
[38] E. Lee, K. A. Persson, *Adv. Energy Mater.* **2014**, *4*, 1400498.
[39] Z. Lun, B. Ouyang, D. A. Kitchaev, R. J. Clément, J. K. Papp, M. Balasubramanian, Y. Tian, T. Lei, T. Shi, B. D. McCloskey, *Adv. Energy Mater.* **2019**, *9*, 1802959.

ADVANCED
SCIENCE NEWS
www.advancedsciencenews.com

ADVANCED
ENERGY
MATERIALS
www.advenergymat.de

[40] Z. Yu, X. Qu, A. Dou, M. Su, Y. Liu, F. Wu, *ACS Appl. Mater. Interfaces* **2019**, *11*, 35777.

[41] M. A. Cambaz, B. P. Vinayan, H. Geßwein, A. Schiele, A. Sarapulova, T. Diemant, A. Mazilkin, T. Brezesinski, R. J. r. Behm, H. Ehrenberg, *Chem. Mater.* **2019**, *31*, 4330.

[42] A. R. Armstrong, P. G. Bruce, *Nature* **1996**, *381*, 499.

[43] A. Urban, A. Abdellahi, S. Dacek, N. Artrith, G. Ceder, *Phys. Rev. Lett.* **2017**, *119*, 176402.

[44] W. Weppner, R. A. Huggins, *J. Electrochem. Soc.* **1977**, *124*, 1569.

[45] H. Xia, L. Lu, G. Ceder, *J. Power Sources* **2006**, *159*, 1422.

[46] G. Hautier, A. Jain, S. P. Ong, B. Kang, C. Moore, R. Doe, G. Ceder, *Chem. Mater.* **2011**, *23*, 3495.

[47] C. Baur, J. Chable, F. Klein, V. S. K. Chakravadhanula, M. Fichtner, *ChemElectroChem* **2018**, *5*, 1484.

[48] M. A. Cambaz, B. P. Vinayan, H. Euchner, S. A. Pervez, H. Geßwein, T. Braun, A. Gross, M. Fichtner, *ACS Appl. Mater. Interfaces* **2019**, *11*, 39848.

[49] A. Jain, S. P. Ong, G. Hautier, W. Chen, W. D. Richards, S. Dacek, S. Cholia, D. Gunter, D. Skinner, G. Ceder, K. A. Persson, *APL Mater.* **2013**, *1*, 011002.

[50] H. Ji, D. A. Kitchaev, Z. Lun, H. Kim, E. Foley, D.-H. Kwon, Y. Tian, M. Balasubramanian, M. Bianchini, Z. Cai, *Chem. Mater.* **2019**, *31*, 2431.

[51] M. Aydinol, A. Kohan, G. Ceder, K. Cho, J. Joannopoulos, *Phys. Rev. B* **1997**, *56*, 1354.

[52] A. O. Kondrakov, A. Schmidt, J. Xu, H. Geßwein, R. Mönig, P. Hartmann, H. Sommer, T. Brezesinski, J. Janek, *J. Phys. Chem. C* **2017**, *121*, 3286.

[53] D. Ensling, G. Cherkashinin, S. Schmid, S. Bhuvaneswari, A. Thissen, W. Jaegermann, *Chem. Mater.* **2014**, *26*, 3948.

[54] A. Abdellahi, A. Urban, S. Dacek, G. Ceder, *Chem. Mater.* **2016**, *28*, 3659.

[55] D.-H. Seo, J. Lee, A. Urban, R. Malik, S. Kang, G. Ceder, *Nat. Chem.* **2016**, *8*, 692.

[56] K. Luo, M. R. Roberts, R. Hao, N. Guerrini, D. M. Pickup, Y.-S. Liu, K. Edström, J. Guo, A. V. Chadwick, L. C. Duda, *Nat. Chem.* **2016**, *8*, 684.

[57] R. A. House, U. Maitra, M. A. Pérez-Osorio, J. G. Lozano, L. Jin, J. W. Somerville, L. C. Duda, A. Nag, A. Walters, K.-J. Zhou, *Nature* **2020**, *577*, 502.

[58] J. Zheng, S. Myeong, W. Cho, P. Yan, J. Xiao, C. Wang, J. Cho, J. G. Zhang, *Adv. Energy Mater.* **2017**, *7*, 1601284.

[59] M. Yoon, Y. Dong, J. Hwang, J. Sung, H. Cha, K. Ahn, Y. Huang, S. J. Kang, J. Li, J. Cho, *Nat. Energy* **2021**, *6*, 362.

[60] Z. Lun, B. Ouyang, D.-H. Kwon, Y. Ha, E. E. Foley, T.-Y. Huang, Z. Cai, H. Kim, M. Balasubramanian, Y. Sun, J. Huang, Y. Tian, H. Kim, B. D. McCloskey, W. Yang, R. J. Clément, H. Ji, G. Ceder, *Nat. Mater.* **2021**, *20*, 214.

[61] J. Lee, D. Yu, Z. Zhu, X. Yao, C. Wang, Y. Dong, R. Malik, J. Li, *ACS Appl. Energy Mater.* **2020**, *3*, 7931.

[62] G. Kresse, J. Furthmüller, *Phys. Rev. B* **1996**, *54*, 11169.

[63] J. P. Perdew, K. Burke, M. Ernzerhof, *Phys. Rev. Lett.* **1996**, *77*, 3865.

[64] S. L. Dudarev, G. A. Botton, S. Y. Savrasov, C. J. Humphreys, A. P. Sutton, *Phys. Rev. B* **1998**, *57*, 1505.

2100204 (12 of 12)

ADVANCED ENERGY MATERIALS

Supporting Information

Determining the Criticality of Li-Excess for Disordered-Rocksalt Li-Ion Battery Cathodes

Jinhyuk Lee,* Chao Wang, Rahul Malik, Yanhao Dong, Yimeng Huang, Dong-Hwa Seo,* and Ju Li*

Supporting Information

Determining the criticality of Li-excess
for disordered-rocksalt Li-ion battery cathodes

Jinhyuk Lee[1,2†*], Chao Wang[1,3†], Rahul Malik[4], Yanhao Dong[1], Yimeng Huang[5],
Dong-Hwa Seo[6*] & Ju Li[1,5*].

[1] Department of Nuclear Science and Engineering, Massachusetts Institute of Technology, Cambridge, MA 02139, USA

[2] Department of Mining and Materials Engineering, McGill University, Montréal, QC H3A 0C5, Canada

[3] School of Materials Science and Engineering, Tongji University, Shanghai 201804, China

[4] CAMX Power LLC, Lexington, MA 02421, USA

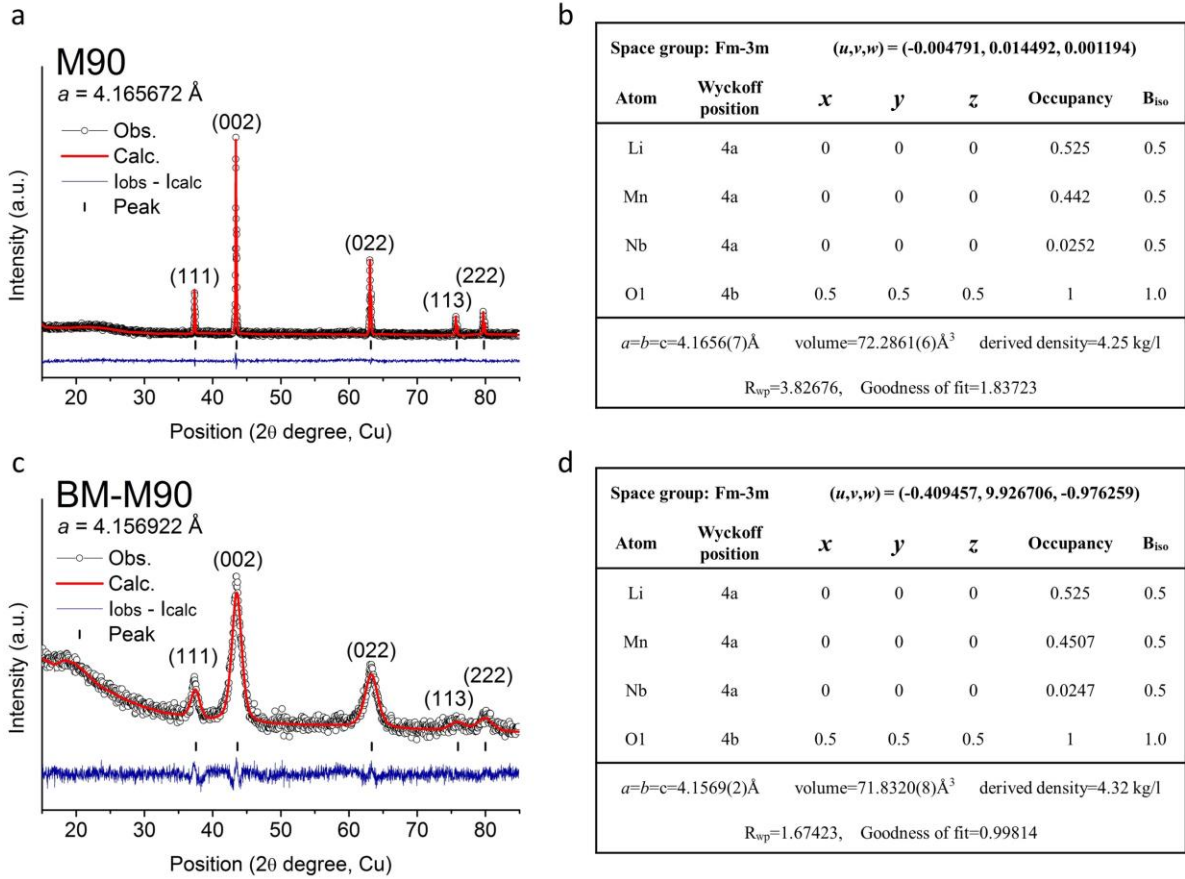[5] Department of Materials Science and Engineering, Massachusetts Institute of Technology, Cambridge, MA 02139, USA

[6] Department of Energy Engineering, School of Energy and Chemical Engineering, Ulsan National Institute of Science and Technology (UNIST), Ulsan, 44919. Republic of Korea

[†] These authors contributed equally to this work.

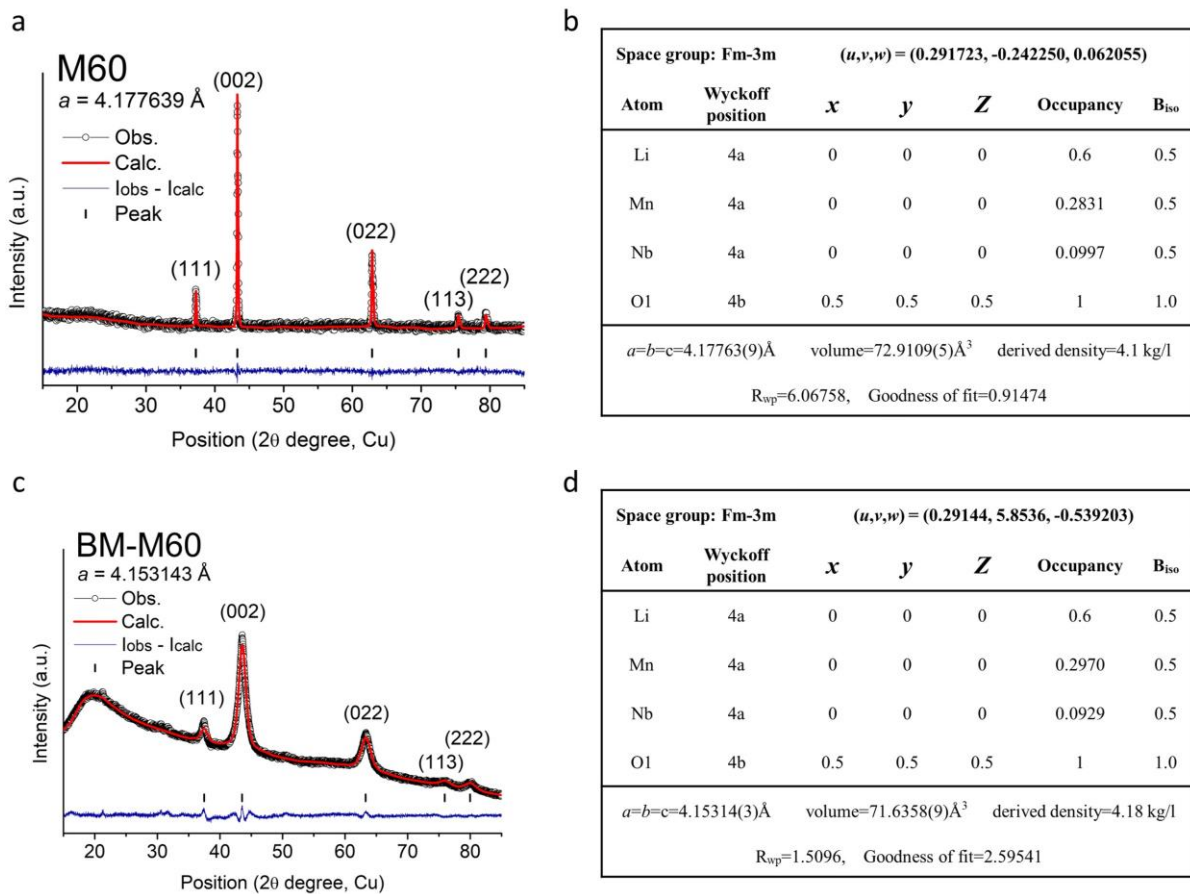[*] Email: liju@mit.edu, jinhyuk.lee@mcgill.ca, dseo@unist.ac.kr

a

M90
$a = 4.165672$ Å

Obs.
Calc.
Iobs - Icalc
Peak

(002)
(022)
(111)
(113)
(222)

Intensity (a.u.)

Position (2θ degree, Cu)
20 30 40 50 60 70 80

b

Space group: Fm-3m		(u,v,w) = (-0.004791, 0.014492, 0.001194)				
Atom	Wyckoff position	x	y	z	Occupancy	B_{iso}
Li	4a	0	0	0	0.525	0.5
Mn	4a	0	0	0	0.442	0.5
Nb	4a	0	0	0	0.0252	0.5
O1	4b	0.5	0.5	0.5	1	1.0

a=b=c=4.1656(7)Å   volume=72.2861(6)Å^3 derived density=4.25 kg/l

R_{wp}=3.82676,   Goodness of fit=1.83723

c

BM-M90
$a = 4.156922$ Å

Obs.
Calc.
Iobs - Icalc
Peak

(002)
(022)
(111)
(113)
(222)

Intensity (a.u.)

Position (2θ degree, Cu)
20 30 40 50 60 70 80

d

Space group: Fm-3m		(u,v,w) = (-0.409457, 9.926706, -0.976259)				
Atom	Wyckoff position	x	y	z	Occupancy	B_{iso}
Li	4a	0	0	0	0.525	0.5
Mn	4a	0	0	0	0.4507	0.5
Nb	4a	0	0	0	0.0247	0.5
O1	4b	0.5	0.5	0.5	1	1.0

a=b=c=4.1569(2)Å   volume=71.8320(8)Å^3 derived density=4.32 kg/l

R_{wp}=1.67423,   Goodness of fit=0.99814

Figure S1. The XRD refinement and structural parameters of the (a, b) as-made and (c, d) ball-milled $Li_{1.05}Mn_{0.90}Nb_{0.05}O_2$ (M90). The crystallographic information file of Fm-3m $LiFeO_2$ (ICSD collection code 51208) was used as an input file. Pseudo Voigt fit was used. The atomic occupancies were initially set to the atomic ratio obtained from elemental analysis, based on which the lattice parameters were first refined. Then, we further refined the lattice parameters and the atomic occupancies simultaneously: transition metal (TM) occupancies were first refined, and then Li occupancy was refined.

2
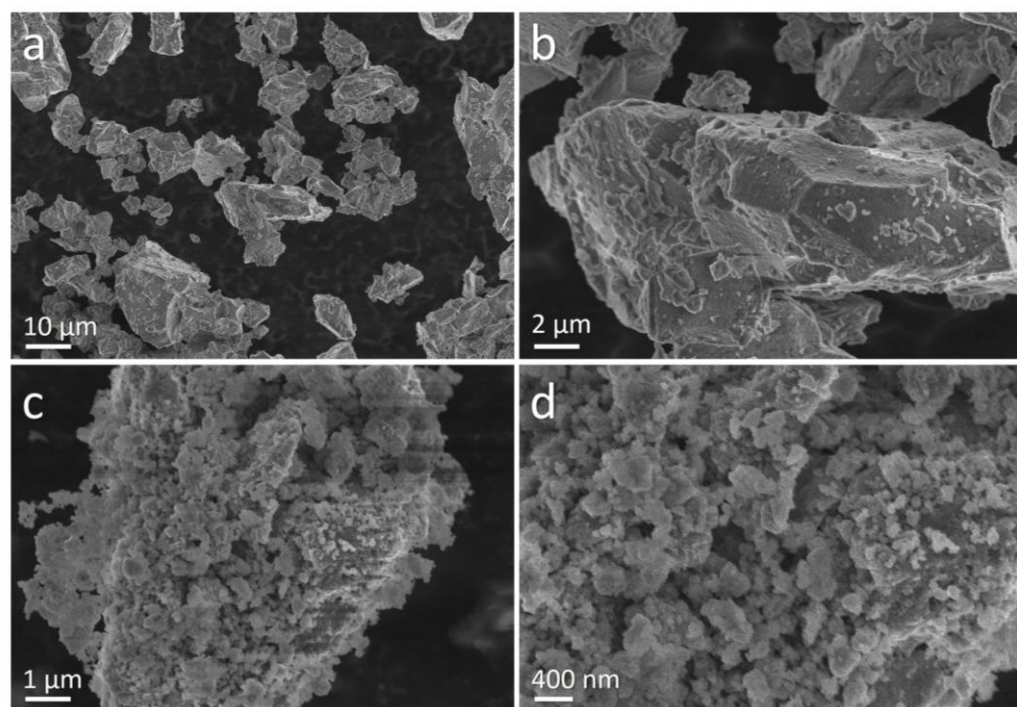
Figure S2. Scanning electron microscopy images of the (a, b) as-made and (c, d) ball-milled M90. The as-made M90 form into 5 μm$<d<$20 μm particles; yet, ball milling pulverizes the particles into $d<$200 nm nanoparticles that loosely segregate into slightly larger particles with varying sizes. This particle size reduction upon ball mill is consistent with the XRD peak broadening after the ball milling.

a M60, $a = 4.177639$ Å. Obs., Calc., Iobs − Icalc, Peak. Peaks labeled (111), (002), (022), (113), (222). Intensity (a.u.) vs Position (2θ degree, Cu).

b

Space group: Fm-3m			(u,v,w) = (0.291723, −0.242250, 0.062055)				
Atom	Wyckoff position	x	y	Z	Occupancy	B_{iso}
Li	4a	0	0	0	0.6	0.5
Mn	4a	0	0	0	0.2831	0.5
Nb	4a	0	0	0	0.0997	0.5
O1	4b	0.5	0.5	0.5	1	1.0

$a=b=c=4.17763(9)$Å volume=72.9109(5)Å³ derived density=4.1 kg/l

R_{wp}=6.06758, Goodness of fit=0.91474

c BM-M60, $a = 4.153143$ Å. Obs., Calc., Iobs − Icalc, Peak. Peaks labeled (111), (002), (022), (113), (222). Intensity (a.u.) vs Position (2θ degree, Cu).

d

Space group: Fm-3m			(u,v,w) = (0.29144, 5.8536, −0.539203)				
Atom	Wyckoff position	x	y	Z	Occupancy	B_{iso}
Li	4a	0	0	0	0.6	0.5
Mn	4a	0	0	0	0.2970	0.5
Nb	4a	0	0	0	0.0929	0.5
O1	4b	0.5	0.5	0.5	1	1.0

$a=b=c=4.15314(3)$Å volume=71.6358(9)Å³ derived density=4.18 kg/l

R_{wp}=1.5096, Goodness of fit=2.59541

Figure S3. The XRD refinement and structural parameters of the (a, b) as-made and (c, d) ball-milled $Li_{1.20}Mn_{0.60}Nb_{0.20}O_2$ (M60). The same refinement protocol as described in the caption of Figure S1 was used.
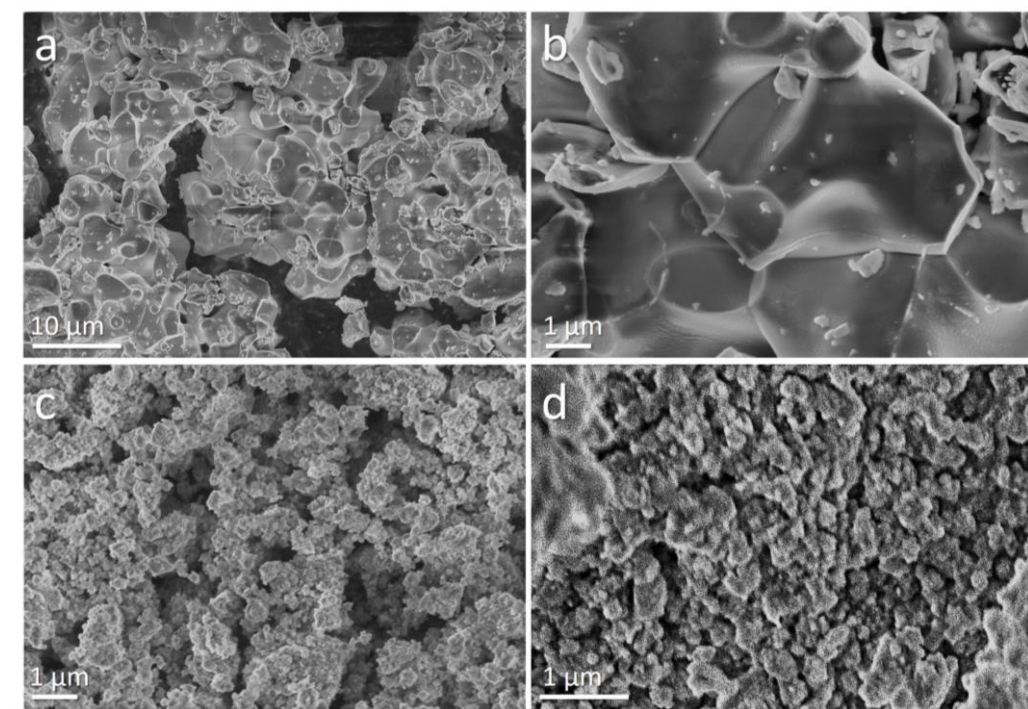
Figure S4. Scanning electron microscopy images of the (a, b) as-made and (c, d) ball-milled M60. As can be seen, the as-made M60 forms into highly agglomerated large particles with $d>10$ µm. After ball milling, the particles are pulverized into $d<200$ nm nanoparticles that loosely form secondary particles with varying degrees of segregation.
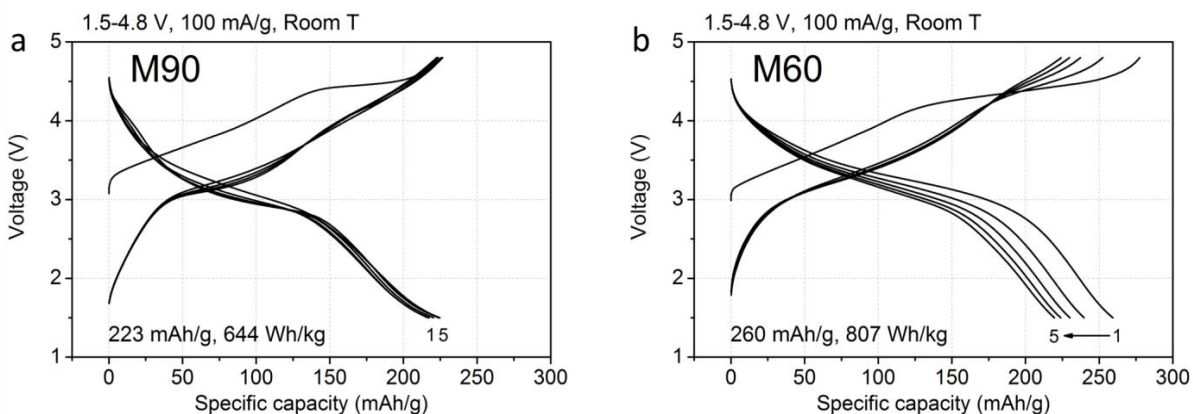
Figure S5. The initial 5-cycles voltage profiles of (a) M90 and (b) M60 when they are cycled between 1.5 V and 4.8 V at 100 mA/g. The capacity fading is seen quite more for M60 than M90. The 40-cycle capacity retention plot is in Fig. 2c in the manuscript.
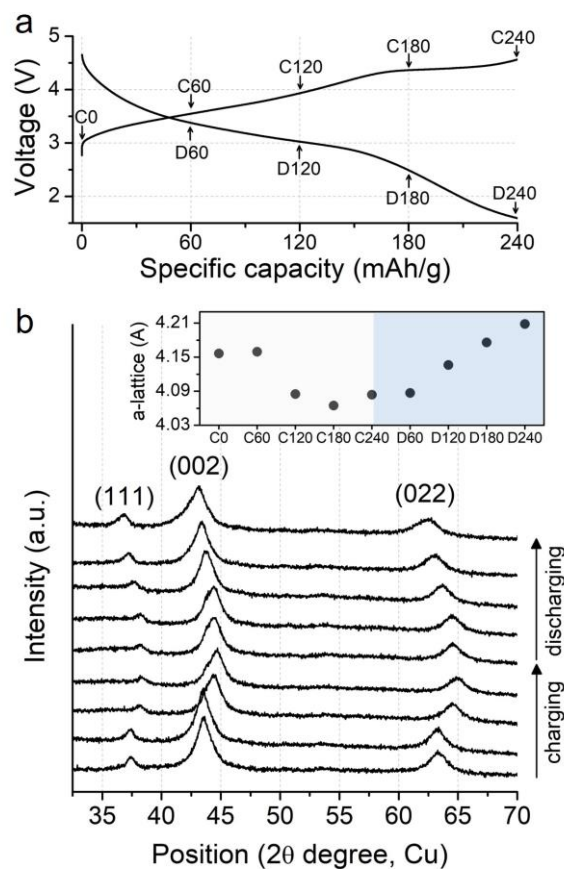
Figure S6. (a) The representative first-cycle voltage profile of M90: The degrees of charging (C0=before cycling, C60=first charge to 60 mAh/g, C120, C180, C240) and discharging (D60=first discharge to 60 mAh/g, D120, D180, D240) are marked for the ex-situ XRD samples. (b) The XRD patterns of the M90 electrode during the first cycle (C0, C60, C120, C180, C240, D60, D120, D180, D240). The inset shows the *a*-lattice parameters of M90 during the test. From the results, we observe a shift of the (111), (002), and (022) Fm-3m XRD peaks to a higher angle upon charging, which recovers upon discharging. This peak-shift reveals that M90's lattice shrinks/expands during the cycling: The inset in Fig. b shows the lattice-parameters obtained from the XRD refinement. The "lattice-breathing" is a typical signature of insertion electrodes, confirming the intercalation reaction of M90.
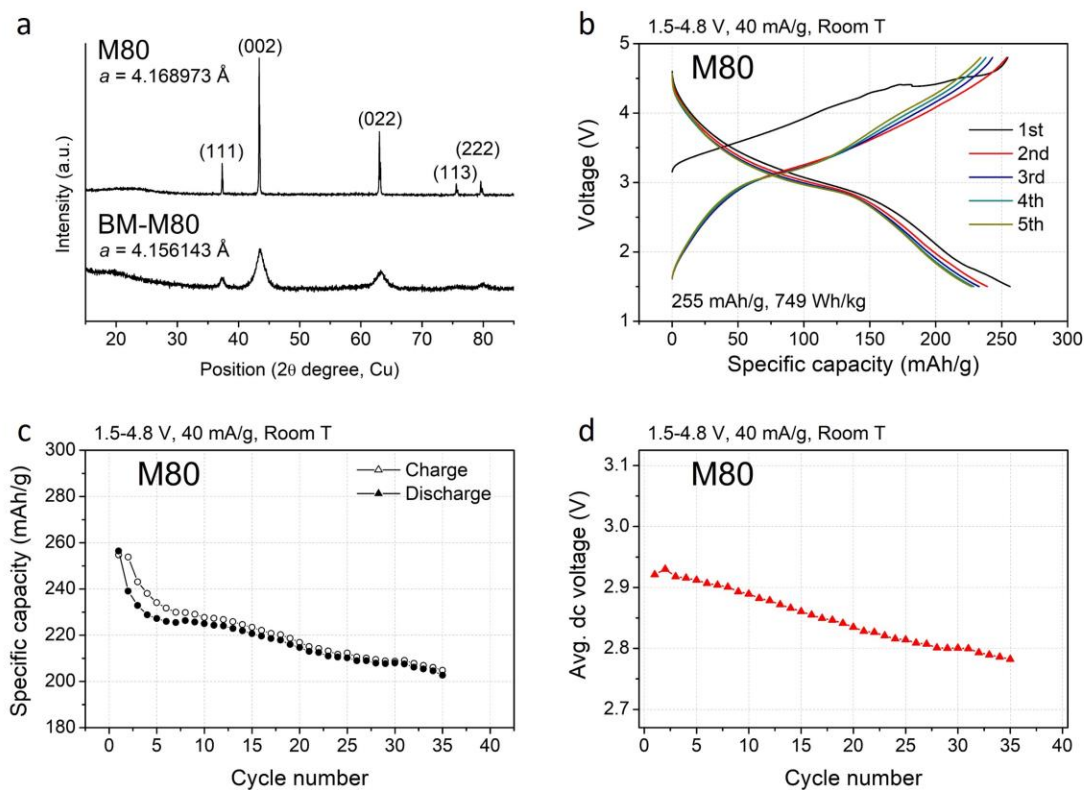
Figure S7. (a) The XRD pattern of $Li_{1.10}Mn_{0.80}Nb_{0.10}O_2$ (M80) before and after ball mill. M80 was synthesized by heating precursors at 1200^oC for 4 hours under Ar atmosphere. (b) The voltage profile of (ball-milled) M80 when cycled between 1.5−4.8 V at 40 mA/g, and the (c) capacity and (d) average discharge voltage retention during the cycling.
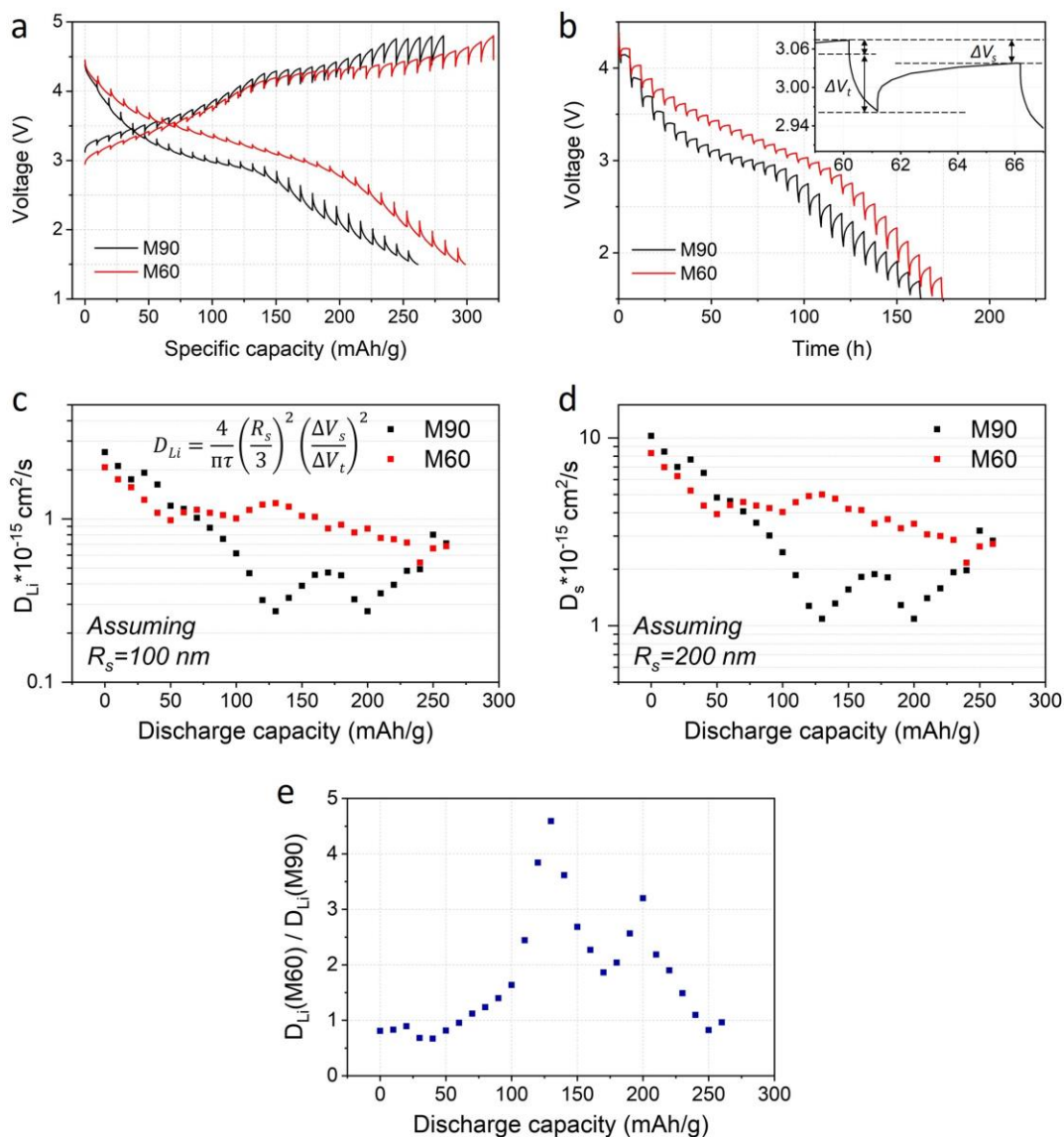
Figure S8. (a) The first charge and discharge profile during the galvanostatic intermittent titration technique (GITT) measurement: we applied 5-hour relaxation after every charging or discharging increment of 10 mAh/g at 20 mA/g. (b) The discharge portion of the GITT profile of M90 and M60, shown as a function of time. The inset reveals a portion from M90, which shows the ΔV_s and ΔV_t, which can be used to estimate the Li diffusivity.[1] The formula used for this derivation is written as the inset. The electrochemistry model leading to this formula assumes spherical electrode particles (radius: R_s) and $D_{Li} \cdot \tau \ll L_s^2$, where τ is the time duration of the pulse, and L_s is the characteristic dimension of the solid-phase material.[1] As the ball-milled M90

and M60 have varying R_s (*i.e.*, not all particles have the same R_s), we derived the Li-diffusivity based on two different assumptions of (c) R_s=100 nm or (d) R_s=200 nm. These R_s values were used because the ball-milled M90 and M60 typically have the (secondary) particle diameter (d=$2R_s$) between 200 nm and 400 nm. In our GITT test, τ is 3600 seconds. (e) The ratio between D_{Li} of M60 and D_{Li} of M90 upon discharge. This ratio does not change with R_s values. From the result, we can see that M60 has higher diffusivity than M90; yet, not the orders of magnitude improvement.
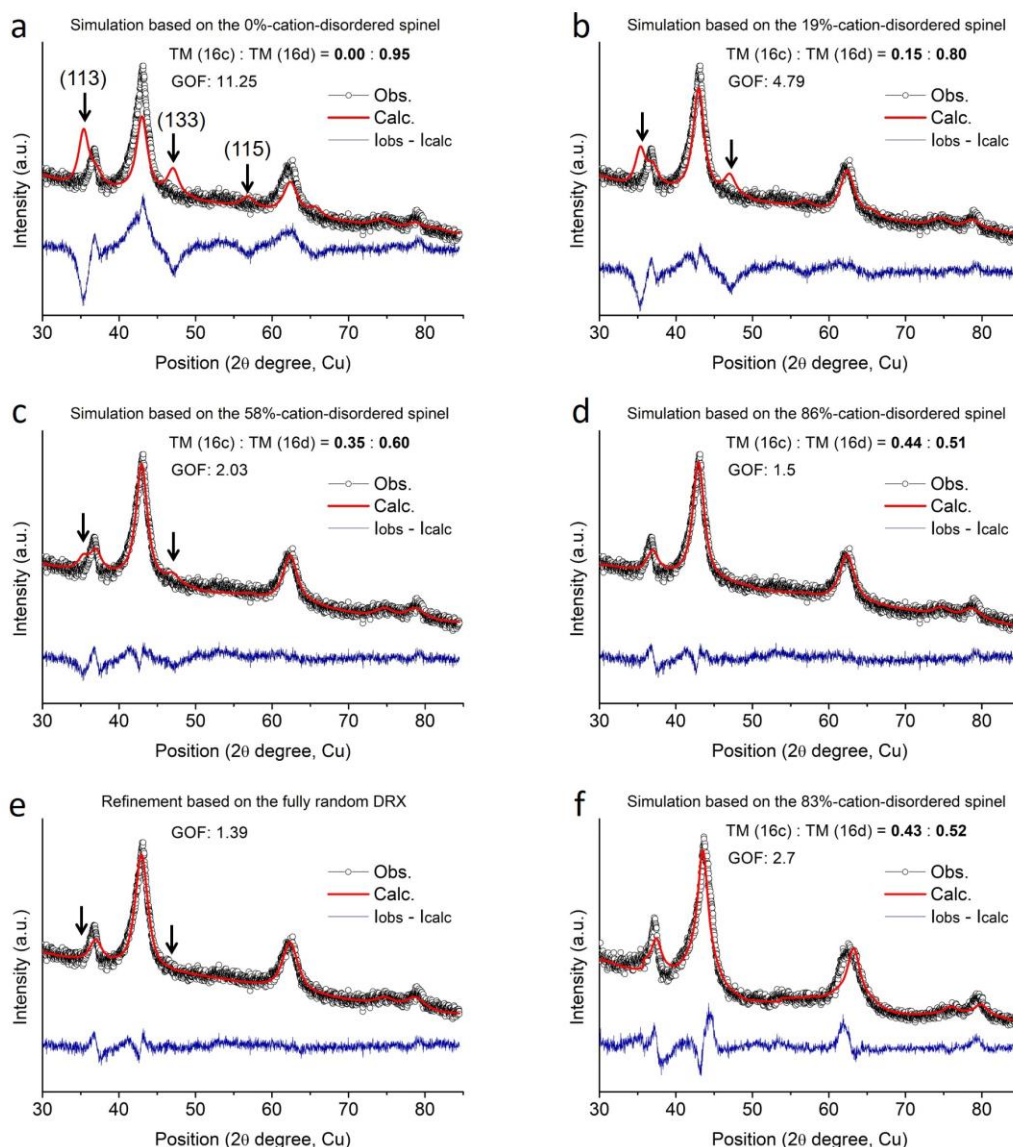
Figure S9. The XRD patterns of M90 (a−e) after the first cycle (1.5−4.8 V, 20 mA/g) and (f) after five cycles compared with the simulated XRD patterns under different assumptions. GOF: goodness of fit.

It is known that highly Mn-rich cathodes such as orthorhombic $LiMnO_2$ can undergo local spinel transformation during extended cycling.[2] M90, as a highly Mn-rich cathode, may also experience a similar transition. In the case of DRX-M90, this local transformation would lead to the phase transition from the "fully random" DRX-structure to DRX with partial spinel-like cation-order (or disordered spinel), as H. Ji *et al.* has shown,[3] which would make the Li-transport property in

M90 better than what would be expected based on the assumption of fully cation-disordered M90. To examine if this DRX-to-spinel transformation upon cycling is the reason for the high capacity of M90, we refined the first-cycled M90's XRD pattern using the similar input file used by Ji *et al.*, which allows us to vary the level of disorder in the spinel structure by changing the TM occupancy in the 16c (0, 0, 0) and 16d (0.5, 0.5, 0.5) sites. In the case of the fully-ordered spinel, all TM-cations sit on the 16d site. We simulated the XRD pattern assuming the TM (16c): TM (16d) occupancy ratio of (a) 0.00: 0.95 [0% cation-disordered spinel, *i.e.*, fully-ordered spinel], (b) 0.15: 0.80 [19% cation-disordered spinel], (c) 0.35: 0.60 [58% cation-disordered spinel], and (d) 0.44: 0.51 [86%-cation-disordered spinel]. Note that the 0.475: 0.475 ratio would be the ratio for the 100% cation-disordered spinel (*i.e.*, fully random DRX). The 0.44: 0.51 ratio was the value obtained after the conventional XRD refinement, while the other simulations (a-c) used the manually fixed occupancy ratio. In this simulation of M90 ($Li_{1.05}Mn_{0.9}Nb_{0.05}O_2$), we did not distinguish Nb from Mn as only 0.05/0.95 TM is Nb. Instead, we assume all TMs are Mn for simplification. Also, we did not try to change the Li occupancies, as the refinement of Li occupancies is known to be highly inaccurate. Thus, we equally distributed the Li to the 16c and 16d sites. Finally, we show the refined XRD pattern using (e) the fully random DRX as the input file. From these results, we can see that the first-cycled M90's XRD pattern cannot be simulated well using the spinel-input file unless we distribute a nearly equal amount of Mn in the 16c sites as in the 16d sites (0.44 vs. 0.51). The 0.44: 0.51 occupancy ratio essentially means that the material is 86% cation-disordered spinel, indicating that the cation distribution is very close to the distribution in the fully random DRX structure (0.475: 0.475) with insignificant spinel-like cation-order. In fact, the first-cycled M90's XRD pattern can easily be simulated with the fully random DRX structure, as shown in Fig. S9e. (f) The XRD refinement shows a similar 83% cation-disordered spinel structure (*i.e.*, 17 % spinel-developed DRX) for M90 after five cycles. According to A. Urban *et al.*, a 86% (or 83%) cation-disordered spinel (or 14% or 17% spinel-developed DRX) would have a nearly identical 0-TM percolation threshold and properties as the fully random DRX-structure.[4] Therefore, we believe it is highly appropriate to discuss the M90's performance based on the simpler percolation theory made for the fully-random DRX material. With this clarification, we can exclude the possibility that rapid DRX-to-spinel-transformation is the main reason for the high capacity of M90 achievable from the beginning of the cycle.
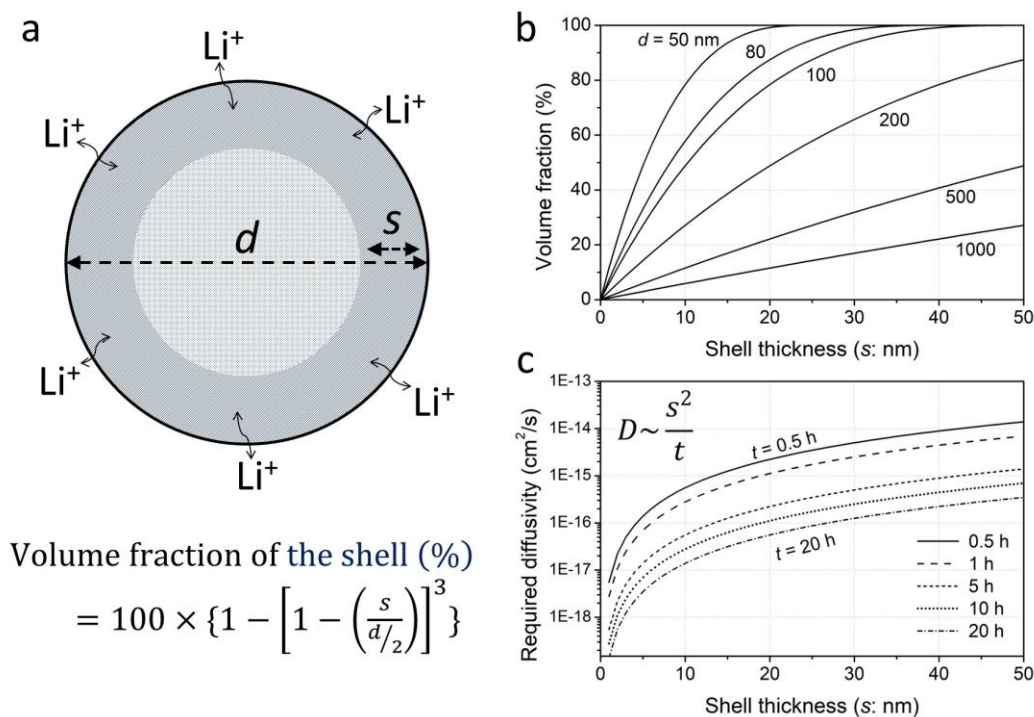
Figure S10. (a) The mathematical model used to calculate the volume fraction of the "Li-travel" shell (thickness: s) within a spherical particle (diameter: d) and (b) its result. (c) The estimation of the Li-diffusivity (cm^2/s) required to travel the particle-shell (thickness: s) at a given time (t) based on the relationship of $s^2 \sim Dt$ from the random walk diffusion model. From these results, we can see that the diffusion length needed to access a significant fraction of Li in a particle (proportional to the specific capacity) becomes exceedingly short as the particle size becomes small. For instance, for a d=80 nm nanoparticle, 20 nm-diffusion would allow nearly 90% of Li in the particle to participate in cycling (Fig. S10b). This shortened diffusion length to access Li in a small-size particle, in turn, renders low Li-diffusivities tolerable for achieving high capacity.

12
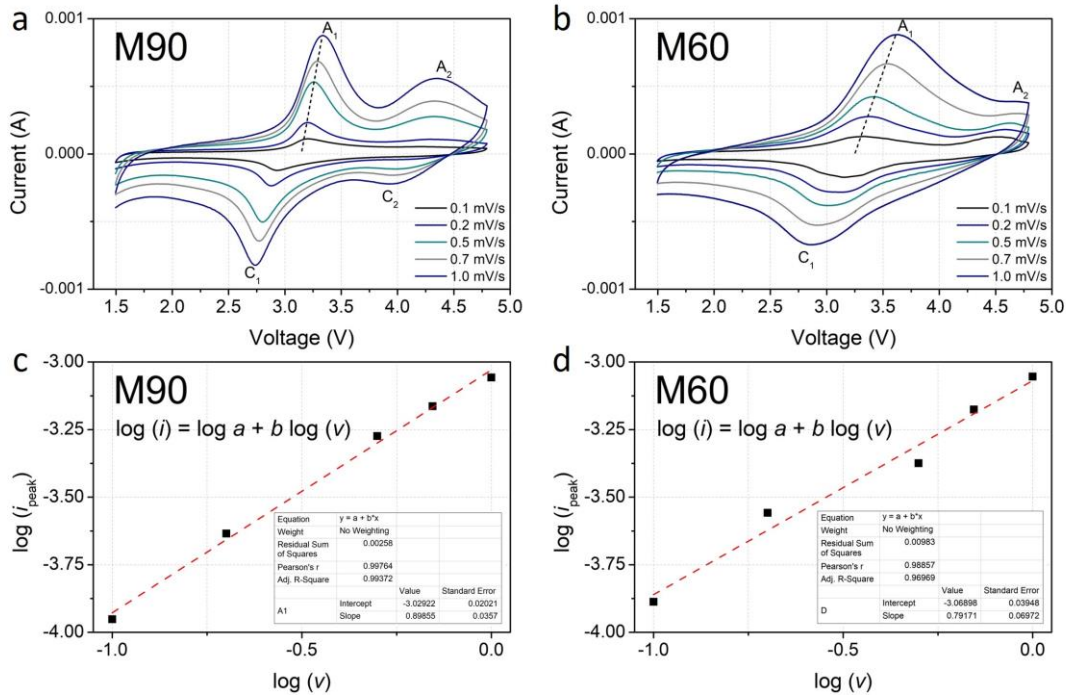
Figure S11. The cyclic voltammetry (CV) profiles of (a) M90 and (b) M60 at different scan rates of 0.1, 0.2, 0.5, 0.7, and 1.0 mV/s. The log (i_{peak}) vs. log (v; rate) plots of (c) M90 and (d) M60. The i_{peak} values for this analysis were obtained from the A_1 anodic current for both M90 and M60.

From the M90's profile (Fig. S11a), we observe two anodic (A_1, A_2) and cathodic (C_1, C_2) peaks, whose intensity increases with a faster scan rate. In the case of M60 (Fig. S11b), two anodic peaks (A_1, A_2) are observed, while the C_2 cathodic peak is not well observed. Certain relationships are known between the scan-rate (v) and current (i) during the CV test, revealing the nature of electrochemical processes. The established relationships are (1) $i = av^1$ (a=constant), which represents a "capacitive" behavior (*i.e.*, non-diffusion-controlled) of electrochemical-double-layer-capacitors (EDLC, *e.g.*, activated carbon) or pseudocapacitors (*e.g.*, RuO_2, MnO_2) and (2) $i = av^{0.5}$ that represents the "diffusion-controlled" behavior of a battery material (*e.g.*, $LiCoO_2$)[2]. When the log i vs. log v plot is drawn, these relationships give the slope (b) of b~1 for capacitors or b~0.5 for battery materials, according to the mathematical operation of:

$$i = a v^b$$

$$\log i = \log a + b \log v$$

13

We find that this i–v relationship for M90 and M60 is similar to that of a capacitor. Fig. S11c and S11d show the log (i_{peak}) vs. log (v) plot of M90 and M60. Here, we collected the i_{peak}-values from the A_1-peak at different rates (v). In the plots, the points fall into a straight line. Linear fitting gives the slope of $b\sim0.89$ for M90 and $b\sim0.79$ for M60; thus, their slope is closer to 1 than 0.5, indicating that the capacitive current is significant during the anodic sweep. We refer to this behavior as "pseudocapacitive" or, to be more specific, "intercalation-pseudocapacitive. Unlike EDLCs that store energy in the electric field (thus non-faradaic), pseudocapacitors utilize fast surface faradaic charge-storage processes. The pseudocapacitance can be further classified into several different types, including (i) redox pseudocapacitance (*e.g.*, MnO_2), which occurs when ions are electrochemically "absorbed" onto the near-surface of materials upon a faradaic charge transfer, and (ii) intercalation pseudocapacitance (*e.g.*, nano-sized TiO_2), which occurs when ions "intercalate" into the tunnels or layers of the electrode material, accompanied by a faradaic charge transfer with no crystallographic phase change.[5] All these capacitances show the slope of b=1 ($b\sim1$); yet, only the intercalation pseudocapacitance exhibits non-negligible redox peaks, which is the case for M90 and M60. Also, the XRD during the cycling of M90 confirms the intercalation behavior (Fig. S6).
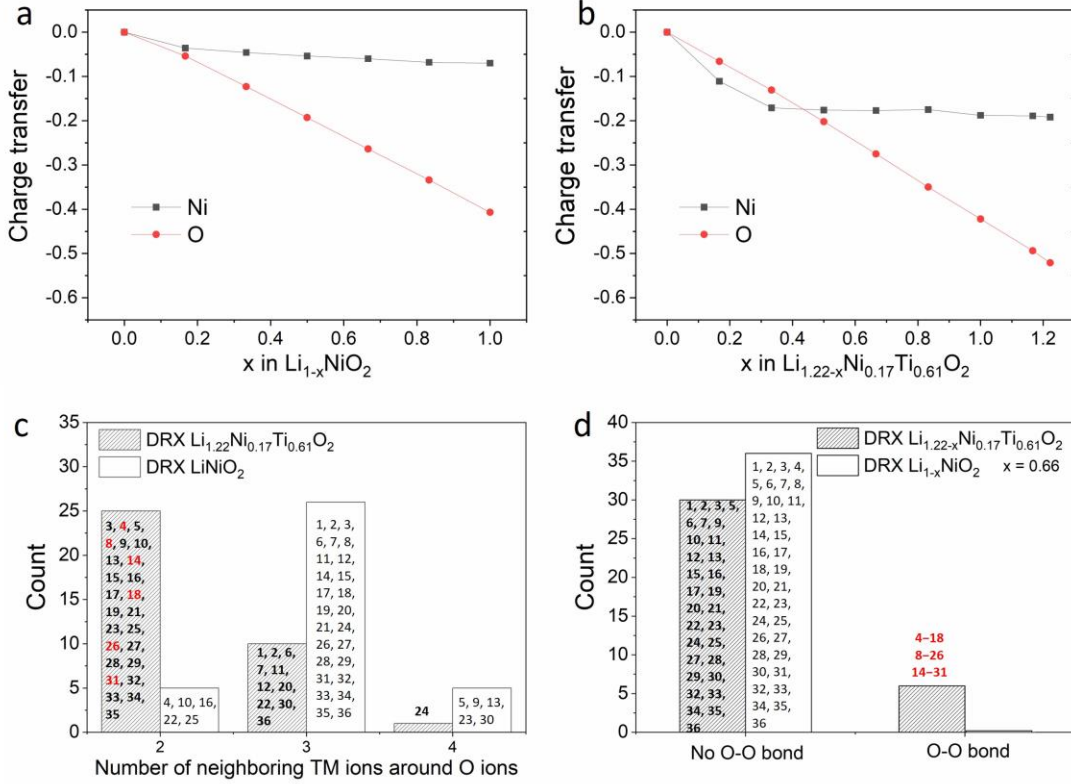
Figure S12. Charge transfer of Ni and O ions in (a) DRX $Li_{1-x}NiO_2$ and (b) DRX $Li_{1.22-x}Ni_{0.17}Ti_{0.61}O_2$. Charge transfer is evaluated by the change of Bader charge with respect to the fully lithiated state (x=0).[6,7] (c) The population of oxygen with respect to the number of neighboring transition metal ions in the supercell of DRX $Li_{1.22}Ni_{0.17}Ti_{0.61}O_2$ and DRX $LiNiO_2$. (d) The population of oxygen with respect to whether it forms O−O bond or not in the supercell of DRX $Li_{1.22-x}Ni_{0.17}Ti_{0.61}O_2$ and DRX $Li_{1-x}NiO_2$ (x = 0.66). The numbers in the histogram indicate the labels of oxygen ions in each supercell. Oxygen ions with red-highlighted numbers form O−O bonds in DRX $Li_{0.66}Ni_{0.17}Ti_{0.61}O_2$. As can be seen, the O−O bond formation occurs between the oxygen ions with a low TM coordination number, indicating that high-Li-excess (low TM-content) facilitates O−O bond formation by allowing oxygens to lose fewer TM−O bonds.
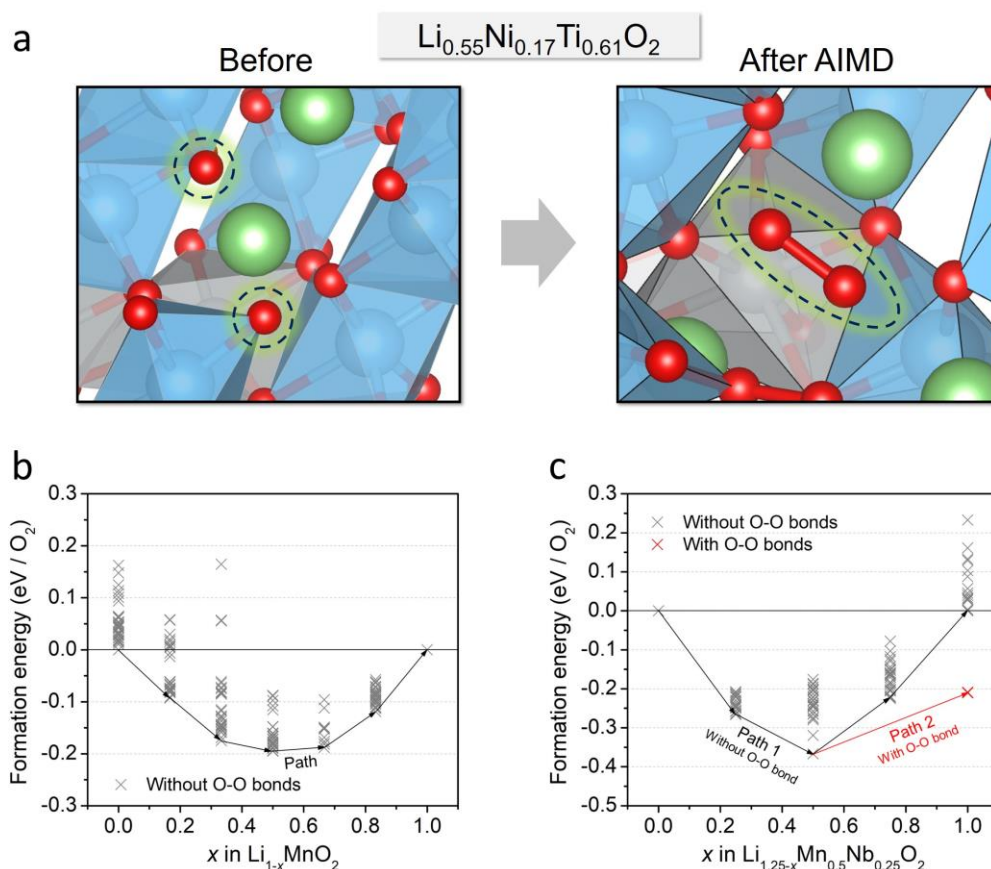
Figure S13. (a) Local structures of DRX-$Li_{0.55}Ni_{0.17}Ti_{0.61}O_2$ before and after AIMD simulation at 1500K. Two oxygen ions apart from each other by 2.71 Å form an O−O bond with the bond distance of 1.29 Å (*i.e.*, superoxide) after the AIMD simulation. Note that some oxygen ions form an O−O bond with the bond distance of ~1.45 Å (*i.e.*, peroxide). (b,c) The DFT formation energies (eV/O_2) of various (b) DRX $Li_{1-x}MnO_2$ and (c) $Li_{1.25-x}Mn_{0.5}Nb_{0.25}O_2$ model structures as a function of the Li-extraction level (*x*). The gray and red points represent the energies of the structures without and with the short O−O bonds (formed upon AIMD simulation at 1500K), respectively. For $Li_{1-x}MnO_2$, the O−O bond did not form during the AIMD simulation. The DFT voltage profile of $Li_{1-x}MnO_2$ in Figure 5e was drawn based on the lowest voltage path designated in Figure b. The DFT voltage profile of $Li_{1.25-x}Mn_{0.5}Nb_{0.25}O_2$ in Figure 5f was based on the two different paths (with or without the O−O bond formation) designated in Figure c.

16

Supplemental methods

Structure preparation for DFT calculations

For calculating the average voltages of layered $LiMO_2$, the hexagonal primitive cell of O3-$LiMO_2$ (space group: $R\bar{3}m$) was adopted for the layered $LiVO_2$, $LiFeO_2$, and $LiCoO_2$, whereas the monoclinic $LiMO_2$ primitive cell (space group: C2/m) was adopted for the layered $LiMnO_2$ and $LiNiO_2$ to consider Mn^{3+} and Ni^{3+} ions' Jahn-teller distortion. For the average voltages of DRX-$LiMO_2$ (M = V, Mn, Fe, Co, Ni), their structures were prepared using Special Quasi-Random Structure (SQS) containing eight formula units of $LiMO_2$.[8] To calculate the voltage profiles of DRX-$LiNiO_2$, DRX-$Li_{1.22}Ni_{0.17}Ti_{0.61}O_2$, and DRX-$LiMnO_2$, large supercells were used to consider various orderings of lithium ions and lithium's vacancy. To determine these large DRX supercells, many cation orderings within a $3 \times 3 \times 2$ supercell containing eighteen formula units of the monoclinic $LiMO_2$ were generated by using the genetic algorithm (GA) method[9] implemented in Atomic Simulation Environment (ASE) package.[10] We fixed a similar cation composition for every layer along the c direction to model DRX structures. The population size of GA was 16, and the first generation of 16 configurations was prepared with randomly arranged cation orderings within the supercell. The energies of every candidate suggested by GA were evaluated using the Ewald summation technique.[11] For each DRX-$LiMO_2$, DRX-$Li_{1.22}Ni_{0.17}Ti_{0.61}O_2$, 7,200 distinct cation orderings were generated, and 30 configurations with lowest electrostatic energies among them were fully relaxed using GGA+U. The configurations with the lowest GGA+U energy were chosen for the ground state DRX structures. The structure of DRX-$Li_{1.25}Mn_{0.5}Nb_{0.25}O_2$ was adopted from the previous computational report.[12]

The lithium and lithium's vacancy orderings were also generated using the GA method due to tremendous amounts of available orderings within a large supercell. We performed same procedures to prepare the ground-state structures of DRX-$Li_{1-x}MO_2$ (M = Ni, Mn, x = 1/6, 1/3, 1/2, 2/3, 5/6, 1) and DRX-$Li_{1.22-x}Ni_{0.17}Ti_{0.61}O_2$ (x = 1/6, 1/3, 1/2, 2/3, 5/6, 1). Due to the small size of the DRX-$Li_{1.25}Mn_{0.5}Nb_{0.25}O_2$ supercell, we enumerated all symmetric distinct lithium and lithium's vacancy orderings for DRX-$Li_{1.25-x}Mn_{0.5}Nb_{0.25}O_2$ (x = 1/4, 1/2, 3/4) and calculated GGA+U energies of 30 configurations for each lithium content.

To prepare the DRX structures with condensed O-species, AIMD simulations were performed with the canonical ensemble (NVT) simulated using a Nosé-Hoover thermostat with a

period of 80 fs. Temperatures were initialized at 100 K and scaled to 1500 K over 400 or 1,400 time steps and hold at 1500 K for 10,000 time steps (20 ps). The initial structures were the ground-state structures of delithiated DRX structures. A plane-wave energy cutoff of 400 eV and a minimal gamma-centered 1 x 1 x 1 k-point grid was used to reduce the computational cost. Twenty configurations were sampled during AIMD simulations at 1500 K and fully relaxed with GGA+U. We excluded the first 1,000 time steps due to the equilibrium procedure and limited one configuration within 400 time steps to get various configurations.

Supporting references

1. Shen, Z., Rahn, C. D. & Wang, C.-Y. Least squares galvanostatic intermittent titration technique (LS-GITT) for accurate solid phase diffusivity measurement. *J. Electrochem. Soc.* **160**, A1842–A1846 (2013).

2. Sato, T., Sato, K, Zhao, W, Kajiya, Y. &Yabuuchi, N. Metastable and nanosize cation-disordered rocksalt-type oxides: revisit of stoichiometric $LiMnO_2$ and $NaMnO_2$. *J, Mater. Chem. A,* **6**, 13943–139514 (2018).

3. Ji, H. et al. Ultrahigh power and energy density in partially ordered lithium-ion cathode materials. *Nat. Energy* **5**, 213–221 (2020).

4. Urban, A., Lee, J. & Ceder, G. The configurational space of rocksalt-type oxides for high-capacity lithium battery electrodes. *Adv. Energy Mater.* **4**, 1400478 (2014).

5. Augustyn, V., Simon, P. & Dunn, B. Pseudocapacitive oxide materials for high-rate electrochemical energy storage. *Energy Environ. Sci.* **7**, 1597–1614 (2014).

6. Henkelman, G., Arnaldsson, A. & Jónsson, Hannes. A fast and robust algorithm for Bader decomposition of charge density. *Computational Materials Science* **36**, 354–360 (2006).

7. McCalla, E., Abakumov, A. M., Saubanère, M., Foix, D., Berg, E. J., Rousse, G., Doublet, M.-L. *et al.* Visualization of OO peroxo-like dimers in high-capacity layered oxides for Li-ion batteries. *Science* **350**, 1516–1521 (2015).

8. Shin, D., Van De Walle, A., Wang, Y. & Liu, Z. K. First-principles study of ternary fcc solution phases from special quasirandom structures. *Phys. Rev. B* **76**, 144204 (2007).

9. Lee, J. *et al.* A new class of high capacity cation-disordered oxides for rechargeable lithium

batteries: Li-Ni-Ti-Mo oxides. *Energy Environ. Sci.* **8**, 3255 (2015).

10. Hjorth Larsen, A. *et al.* The atomic simulation environment - A Python library for working with atoms. *J. Phys.: Condens. Matter* **29**, 273002 (2017).

11. Toukmaji, A. Y. & Board, J. A. Ewald summation techniques in perspective: A survey. *Computer Physics Communications* **95**, 73−92 (1996).

12. Seo, D.-H. *et al.* The structural and chemical origin of the oxygen redox activity in layered and cation-disordered Li-excess cathode materials. *Nat. Chem.* **8**, 692–697 (2016).